Article

Cell Reports

Microglia-Triggered Plasticity of Intrinsic Excitability Modulates Psychomotor Behaviors in Acute Cerebellar Inflammation

Graphical Abstract

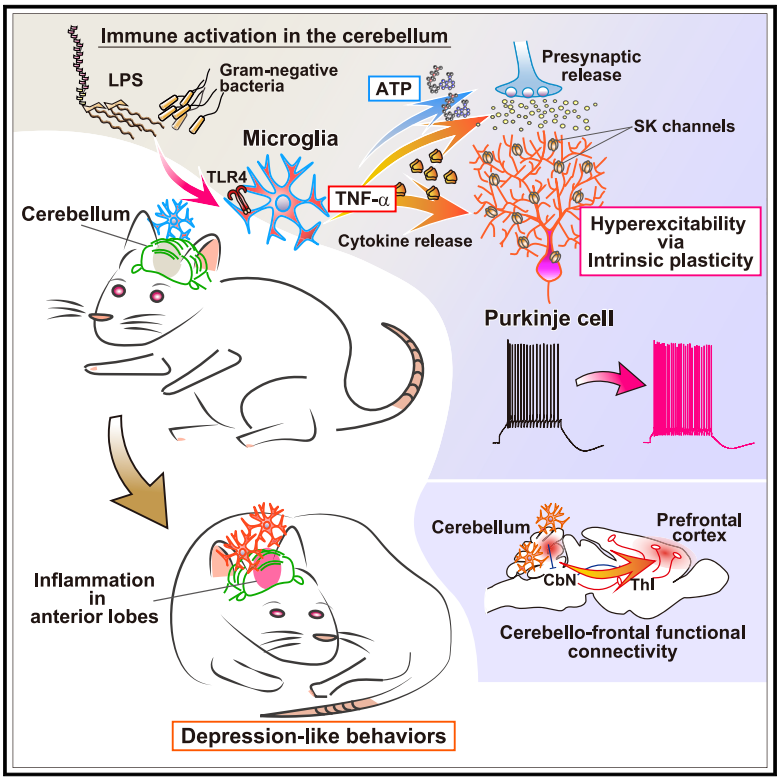

Highlights

- Purkinje cell-intrinsic plasticity is induced by TNF-α released from microglia
- TNF-α and ATP following microglial activation facilitate synaptic transmission
- Acute inflammation in the anterior cerebellum resulted in depression-like behaviors
- Suppression of microglia rescued both hyperexcitability and behavioral modulation

Authors

Masamichi Yamamoto, Minsoo Kim, Hirohiko Imai, Yamato Itakura, Gen Ohtsuki

Correspondence

gohtsuki@neurosci.biophys.kyoto-u.ac.jp

In Brief

Yamamoto et al. find that during acute inflammation in the cerebellum, both non-synaptic (intrinsic excitability) and synaptic plasticity are induced by inflammatory cytokines released from microglia via TLR4 pathways. A battery test of animal behaviors and rs-fMRI suggest a reduction of animal behavior and abnormal brain functional connectivity, which immune suppression recovered.

Yamamoto et al., 2019, Cell Reports *28*, 2923–2938
September 10, 2019
https://doi.org/10.1016/j.celrep.2019.07.078

CellPress

Cell Reports
Article

Microglia-Triggered Plasticity of Intrinsic Excitability Modulates Psychomotor Behaviors in Acute Cerebellar Inflammation

Masamichi Yamamoto,[1,6] Minsoo Kim,[2,3,6] Hirohiko Imai,[4,6] Yamato Itakura,[5] and Gen Ohtsuki[2,5,7,*]
[1]Department of Nephrology, Kyoto University Graduate School of Medicine, Kyoto University Hospital, Shogoin-Kawaramachi-cho, Sakyo-ward, Kyoto 606-8507, Japan
[2]The Hakubi Center for Advanced Research, Kyoto University, Yoshida, Sakyo-ward, Kyoto 606-8501, Japan
[3]Department of Molecular and Cellular Physiology, Kyoto University Graduate School of Medicine, Yoshida-Konoe-cho, Sakyo-ward, Kyoto 606-8501, Japan
[4]Department of Systems Science, Kyoto University Graduate School of Informatics, Yoshida-Honmachi, Sakyo-ward, Kyoto 606-8501, Japan
[5]Department of Biophysics, Kyoto University Graduate School of Science, Kitashirakawa-Oiwake-cho, Sakyo-ward, Kyoto 606-8502, Japan
[6]These authors contributed equally
[7]Lead Contact
*Correspondence: gohtsuki@neurosci.biophys.kyoto-u.ac.jp
https://doi.org/10.1016/j.celrep.2019.07.078

SUMMARY

Cerebellar dysfunction relates to various psychiatric disorders, including autism spectrum and depressive disorders. However, the physiological aspect is less advanced. Here, we investigate the immune-triggered hyperexcitability in the cerebellum on a wider scope. Activated microglia via exposure to bacterial endotoxin lipopolysaccharide or heat-killed Gram-negative bacteria induce a potentiation of the intrinsic excitability in Purkinje neurons, which is suppressed by microglia-activity inhibitor and microglia depletion. An inflammatory cytokine, tumor necrosis factor alpha (TNF-α), released from microglia via toll-like receptor 4, triggers this plasticity. Our two-photon FRET ATP imaging shows an increase in ATP concentration following endotoxin exposure. Both TNF-α and ATP secretion facilitate synaptic transmission. Region-specific inflammation in the cerebellum *in vivo* shows depression- and autistic-like behaviors. Furthermore, both TNF-α inhibition and microglia depletion revert such behavioral abnormality. Resting-state functional MRI reveals overconnectivity between the inflamed cerebellum and the prefrontal neocortical regions. Thus, immune activity in the cerebellum induces neuronal hyperexcitability and disruption of psychomotor behaviors in animals.

INTRODUCTION

Excessive activation of microglia—the resident immune cells of the CNS—causes neuroinflammatory responses following immune challenges in the brain. Although accumulating evidence supports a notion that microglia are associated not only with inflammation, consisting of "tumor, rubor, calor, et dolor (tumor, blush, heat, and pain)" because of microbial pathogens, but also with emotional or mood-related psychiatric diseases, accompanied by psychological stress or morbidity, the full physiological effects of immune-related responses on the CNS remain unclear (Saijo and Glass, 2011; Aguzzi et al., 2013; Yirmiya et al., 2015; Xanthos and Sandkühler, 2014; Chung et al., 2015; Tay et al., 2017; Paolicelli et al., 2011; Parkhurst et al., 2013; Prinz and Priller, 2017).

Previous reports showed that transient exposure of hippocampal slices to the Gram-negative bacterial endotoxin lipopolysaccharide (LPS) activates microglia, and it increases in the presynaptic release of excitatory transmitter (Pascual et al., 2012). Exposure to LPS also depresses the postsynaptic efficacy of glutamate receptors under conditions of low oxygenation (Zhang et al., 2014). In these studies, activated microglia release ATP and reactive oxygen species, resulting in the induction of synaptic plasticity. Inflammatory cytokines are also known to modulate synaptic transmission (Beattie et al., 2002; Pribiag and Stellwagen, 2013; Santello et al., 2011; Habbas et al., 2015). In contrast, CNS neurons exhibit a form of non-synaptic plasticity that enables them to modify intrinsic membrane properties in response to external activity. In addition, neurons change the firing pattern and the membrane excitability of dendrites over the long term. Independent from synaptic plasticity, changes in the intrinsic excitability of neurons may provide a second type of plasticity, which relates to learning and memory engrams (Marder et al., 1996; Hansel et al., 2001; Daoudal and Debanne, 2003). A hypothesis has suggested that synaptic plasticity primarily establishes connectivity patterns among neurons through structural changes in synapses, whereas plasticity of intrinsic excitability provides the main mechanism for integrating neurons into active engrams. It may establish functional connectivity between brain regions and may modulate animal behavior (Titley et al., 2017). Several reports showed that activated microglia alter non-synaptic membrane excitability in neurons and synaptic transmission via tumor necrosis factor (TNF) alpha in the neocortex or hippocampus (Gao et al., 2014; Klapal et al., 2016; Kato et al., 2016; Tzour et al., 2017); however, direct evidence regarding

the long-term plasticity of intrinsic excitability via microglia, the mechanisms at the cellular level, and the relevance to animal diseases is lacking. Thus, whether microglia drive the activity pattern of neurons in which neuroinflammation occurs in a brain is not well understood.

In the cerebellum, Purkinje cells are the principal output neurons and have primary dendrites with highly arborized branches. A characteristic response pattern of spike firing without glutamatergic-fiber projections (i.e., parallel fiber and climbing fiber) is determined by the intrinsic membrane properties derived from various active ion channels (Raman and Bean, 1999), including Ca^{2+}-activated potassium (K^+) channels (Womack and Khodakhah, 2002, 2004). Purkinje cells show an activity-dependent increase in spike firing through of the modulation of intrinsic membrane properties (Belmeguenai et al., 2010; Ohtsuki et al., 2012; Grasselli et al., 2016; Ohtsuki and Hansel, 2018). This long-lasting form of excitability changes is called intrinsic plasticity. Intrinsic plasticity is induced via both the phosphatase-dependent signaling and the downregulation of small conductance Ca^{2+}-activated K^+ channels (SK channels), associated with the increase in the excitability of dendrites. Voltage-gated K^+ channel (Kv)-, SK-, and large-conductance Ca^{2+}-activated K^+ channel BK-type K^+ channels are known to actively dampen back-propagation of somatic sodium spikes in dendrites (Martina et al., 2003; Rancz and Häusser, 2006; Ohtsuki et al., 2012). Hyperpolarization of membrane potential of Purkinje cells improves the propagation of action potential through the axon with high fidelity, up to ~260 Hz (Monsivais et al., 2005). The output firing pattern of Purkinje cells is translated into intense inhibition to the cerebellar nuclei (CbN) as rebound potentials followed by spike bursting (Zheng and Raman, 2010). Spike bursting in the CbNs is correlated to ongoing locomotion *in vivo* (Sarnaik and Raman, 2018). Therefore, changes in the firing pattern of cortical Purkinje cells (e.g., via intrinsic plasticity) plausibly modulate animal behavior (Schonewille et al., 2010). However, the projected regions from cerebellar cortex into the CbNs are specifically distinguished among dentate, fastigial, and interposed nuclei (Bagnall et al., 2009). Among these regions, the fastigial nuclei are assumed to be involved with autonomic disturbance and related behaviors. For example, the electrical stimulation of the rostral fastigial nuclei elicits hypertension and offensive behaviors of animals (Reis et al., 1973). Given that microglia activation in the cerebellar cortex induces hyperexcitability of output neurons through intrinsic plasticity, it is assumed that the cerebellar region-specific inflammation can modulate animal behaviors, relating to the corresponding projection region in the CbNs.

Invasion of bacterial product into brain disturbs its function through excessive immune responses (Yirmiya et al., 2015). In the present study, we investigated whether microglia, activated by exposure to bacterial endotoxin or heat-killed bacteria, modulate cerebellar neuronal excitability. In addition, we aimed to elucidate the induction mechanism of excitability plasticity. Furthermore, we examined the effect of aberrant neuronal excitability on animal behavior and functional connectivity during the acute state of cerebellar inflammation in individual regions, and we challenged whether the symptoms of acute cerebellitis could be rescued.

RESULTS

Microglia Modulate the Intrinsic Excitability of Cerebellar Purkinje Neurons

To investigate the nature of immune-neuron interactions, we examined the neuronal excitability of Purkinje cells under slice preparation following exposure to the endotoxin LPS (10–12 μg/mL), an outer membrane component of Gram-negative bacteria, which activate microglia. LPS was applied to cerebellar slices in a bath chamber. After that, we examined the firing properties of Purkinje neurons by whole-cell patch-clamp recording and under current clamp (Figures 1A and 1B). The firing frequency of neurons in response to depolarization with different current pulses was significantly higher after LPS application than under control conditions. To investigate the time course of firing changes, we subjected slices to transient LPS exposure; then, we continuously monitored subsequent firing properties for more than 30 min. Firing frequency was significantly higher relative to baseline following LPS exposure compared with control ($^*p < 0.001$) (Figures 1C and 1D). The tendency toward a correlation between original excitability and change in excitability was not prominent (pairwise correlation coefficient = 0.176, n = 8), implying that firing changes are not biased toward the original state of the neurons. The duration of this plasticity was more than 70 min ($^*p < 0.05$) (Figure S1A). Following our series studies (Belmeguenai et al., 2010), we monitored the firing property under suppression of γ-aminobutyric acid A ($GABA_A$) receptor activity, using 100 μM picrotoxin throughout the study, except for as shown in Figure S1A.

We next applied heat-killed Gram-negative bacteria (Figure 1E). Because the LPS is the extract of Gram-negative bacteria, it is necessary to clarify whether the invasion of the Gram-negative bacteria may modulate the neural excitability. After treatment with heat-killed *Escherichia coli* (*E. coli*) *0111:B4* (HKEB) or heat-killed *Pseudomonas aeruginosa* (HKPA) (10^7 cells/mL), treated neurons exhibited significantly higher firing frequencies than control neurons. However, exposure to Gram-positive bacteria (heat-killed *Streptococcus pneumoniae* [HKSP]), which have no LPS, did not lead to significant increases in firing of Purkinje neurons. Results from long-term recordings indicated an increase in firing frequency following exposure to heat-killed Gram-negative bacteria (Figures 1F and 1G) (HKEB and HKPA, $^*p < 0.03$), but not Gram-positive bacteria (HKSP, $p > 0.1$). Action potential waveforms also suggested that neurons showed enhanced excitability following endotoxin exposure (Table S1). Another major cell-wall component derived from *E. coli*, peptidoglycan, did not significantly alter the waveforms (Table S1). Experiments with 2,3-dioxo-6-nitro-1,2,3,4-tetrahydrobenzo[*f*]quinoxaline-7-sulfonamide (NBQX) suggested that this firing plasticity was induced without the involvement of α-amino-3-hydroxy-5-methyl-4-isoxazolepropionic acid receptor (AMPA) receptors ($^*p < 0.05$) (Figure S1B). Therefore, our findings suggest that exposure to endotoxin substantially altered the intrinsic membrane excitability of Purkinje neurons.

Previously, Belmeguenai et al. (2010) demonstrated that Purkinje cells exhibit intrinsic plasticity, which is defined as an increase in firing frequency lasting more than 30 min. Simultaneous somato-dendritic recordings demonstrated enhancement

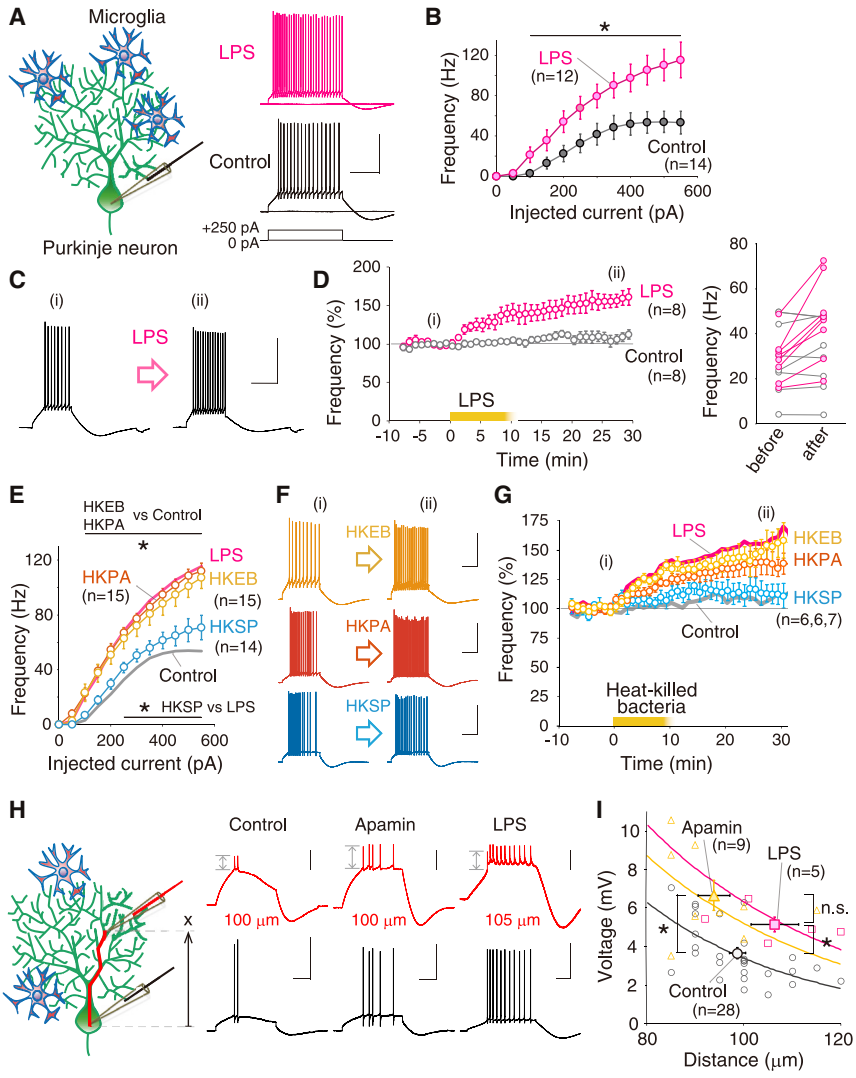

Figure 1. Exposure to Bacterial Endotoxin Alters Excitability in Cerebellar Neurons

(A) Representative action potential (AP) firings of control neurons and Purkinje neurons treated with lipopolysaccharide (LPS) (10–12 μg/mL) in response to depolarization pulses.

(B) Firing frequency in response to depolarization pulses. Data suggest an increase in firing frequency following bath application of LPS.

(C and D) Representative AP firing before (i) and after (ii) LPS exposure, and time courses of the normalized frequency. Representative AP traces in (C) were obtained from the corresponding time points in (D). Averaged firing frequency of each Purkinje cell before and after the LPS exposure (magenta) is plotted in the right graph with control (gray), suggesting the possibility of frequency increase in a broad range.

(E) Bath application of heat-killed Gram-negative bacteria (10^7 cells/mL, HKEB [heat-killed *Escherichia coli* 0111:B4] and HKPA [heat-killed *Pseudomonas aeruginosa*]), but not Gram-positive bacteria (HKSP [heat-killed *Streptococcus pneumoniae*]), increases firing frequency. The firing frequency in response to depolarization pulses is shown (HKEB, orange; HKPA, red; HKSP, blue).

(F and G) Representative firing (F) and normalized time courses (G) of long-lasting recordings of HKEB, HKPA, and HKSP application.

(H) Representative AP firings from soma (black) and dendrite (red). The distance of dendrite patching (X) is shown below each trace.

(I) Distance-voltage plot of back-propagated APs (control, black; LPS, magenta; apamin, orange). *$p < 0.05$, two-tailed Mann-Whitney U test. bAP voltage exponentially attenuates through approximate curves along the length of the dendrite process (Ohtsuki et al., 2012).

Data are represented as mean ± SEM. Time courses of the change in firing frequency were normalized between −5 and −1 min in (D) and (G). Reagent application began at 0 min and continued for 10 min. Scales: 40 mV and 200 ms (A, C, and F) and 5 mV (bar scales) and (right-angle scales) 40 mV and 100 ms (H). See also Figure S1 and Table S1.

of dendritic excitability accompanied by intrinsic plasticity (Ohtsuki et al., 2012; Ohtsuki and Hansel, 2018). These increases in firing frequency and dendritic excitability are induced by transient depolarization of the neuronal membrane via both phosphatase-dependent signaling and downregulation of SK channels. Findings from Purkinje cell-specific conditional knockout mice for protein phosphatase (PP) 2B suggest that induction of intrinsic plasticity occurs through PP2B molecules (Schonewille et al., 2010). Here, we monitored intrinsic plasticity induction by 5-Hz somatic depolarization after exposure to LPS (Figure S1C), and we found that intrinsic plasticity was occluded in such a condition. LPS exposure before 5-Hz depolarization conditioning prevented the induction of intrinsic plasticity. We also monitored the firing pattern in response to LPS exposure under blockade of the SK channels by apamin (Figure S1D); here, the LPS-triggered firing increase was impaired. Results of both occlusion of intrinsic plasticity induction by pre-exposed LPS (Figure S1C) and impairment of LPS-triggered intrinsic plasticity induction under SK-channel blockade (Figure S1D) suggest that the firing increase following endotoxin exposure was induced by the same molecular signaling for intrinsic plasticity (Belmeguenai et al., 2010). The suppression of intraneuronal Ca^{2+} and PPs PP1, PP2A, and PP2B impaired the induction of plasticity (Figures S1E–S1G). These results suggest that the firing-increased plasticity by LPS is mediated by intraneuronal Ca^{2+} and PPs.

We next investigated changes in action potentials on both soma and dendrites after LPS application (Figures 1H and 1I). The amplitude of the back-propagated action potentials (bAPs) in Purkinje cell dendrites was increased and accompanied by intrinsic plasticity induction (Ohtsuki et al., 2012; Ohtsuki and Hansel, 2018). Here, we applied somatic depolarization pulses under control conditions, in the presence of the SK-channel blocker, and after LPS exposure. bAP voltage on dendrites was significantly increased following LPS administration (*$p < 0.04$), relative to those under SK-channel blockade

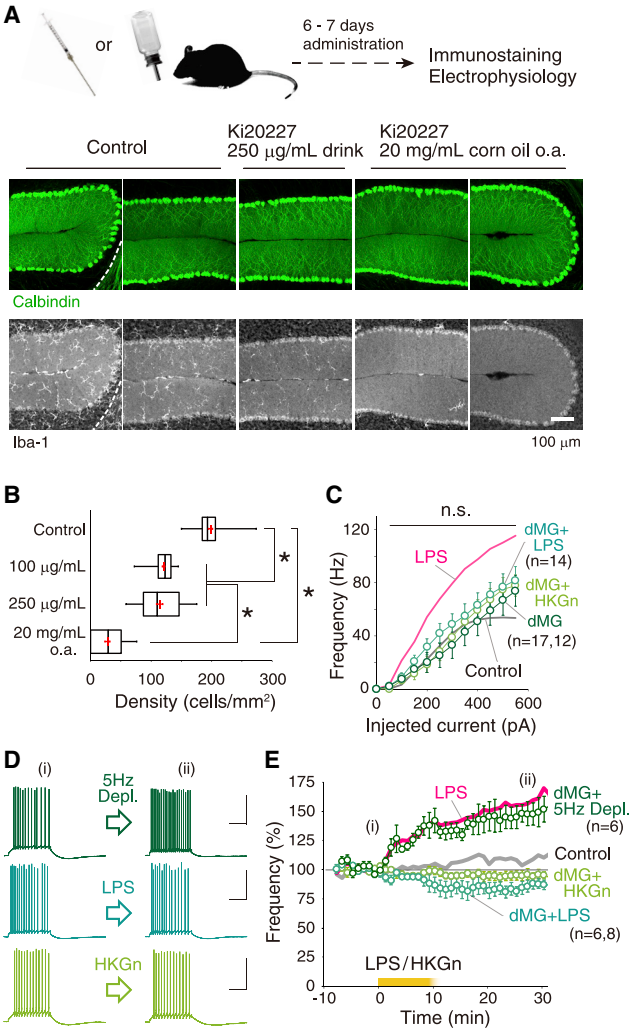

Figure 2. Depletion of Microglia Abolished the Excitability Plasticity in Purkinje Neurons in Mice

(A) Depletion of microglia by Ki20227 administration for a week in C57BL/6J mice. Different concentrations of Ki20227 were given. o.a., oral administration.

(B) Density of microglia of control and Ki20227-administered cerebella. *p < 0.05, Kruskal-Wallis test. Results of 100 and 250 μg/mL and of 20 mg/mL of Ki20227 administration and control are shown.

(C) Suppression of the increase in firing frequency by exposure to lipopolysaccharide (LPS) and HKGn (heat-killed Gram-negative bacteria mixture: HKEB+HKPA). The firing frequency in response to depolarization pulses is shown. n.s., not significant; p > 0.05, two-tailed Mann-Whitney U test.

(D and E) Impairment of the excitability increase by exposure to LPS and HKGn in the microglia-depleted cerebella. Representative firing (D) and normalized time courses (E) of long-lasting recordings are shown. Intrinsic plasticity was induced by 5-Hz depolarization (at 0 min) of Purkinje neurons in microglia-depleted cerebella (dMG+5Hz Depl.).

Data are represented as mean ± SEM. Time courses of the change in firing frequency were normalized between −5 and −1 min in (E). Reagent application began at 0 min and continued for 10 min. Scales: 40 mV and 200 ms (D). See also Figure S2 and Table S2.

(*p < 0.002), in a distance-dependent manner along the soma-dendrite axis (Figure 1I). The extent of the bAP increase by exposure to LPS and apamin was similar, which suggests that microglia activation enhances excitability at dendrites via downregulation of SK2 channels.

Given that microglia were the trigger for the excitability increase, elimination of microglia may block this plasticity. To deplete microglia in living animals, we administered the colony-stimulating factor 1 receptor (CSF1R) kinase inhibitor Ki20227 (Elmore et al., 2014; Ohno et al., 2006; see also Nakayama et al., 2018). Following continuous oral administration of Ki20227 or with drink in three concentrations, the number of microglia in the immunostained cerebellar cortex was reduced to 14% at maximum (*p < 0.00001, multiple comparison) (Figures 2A, 2B, and S2A–S2F). Therefore, our Ki20227 administration depleted almost all microglia in the cerebellum. Then, we examined the neuronal excitability in the microglia-depleted cerebella and found no increase in firing against exposure to both LPS and heat-killed Gram-negative bacteria mixture (HKEB+HKPA) (Figure 2C). Long-term recordings also showed that exposure to LPS and heat-killed Gram-negative bacteria no longer increased frequency (LPS, *p < 0.05 of reduction; heat-killed Gram-negative bacteria, p > 0.3), whereas innate firing frequency increased after 5-Hz conditioning for intrinsic plasticity (*p < 0.05) (Figures 2D and 2E). These results indicate that microglia are involved in increasing the excitability of cerebellar neurons, which is supported by results of co-application with minocycline, an inhibitor of microglial activity (p > 0.7) (Figures S2G and S2H).

Involvement of Inflammatory Cytokine in the Excitability Plasticity

A possible mechanism for microglia-triggered neural hyperexcitability is mediated by inflammatory cytokines, including TNF-α, interleukin (IL)-6, and IL-1β. Among them, TNF-α is released in the earliest phase of immune-cell stimulation. We first examined the firing frequency of neurons treated with TNF-α. Firing frequency of TNF-α-treated neurons was significantly higher than in control or peptidoglycan-treated neurons (Figures 3A and 3B). In addition, co-application of LPS or heat-killed Gram-negative bacteria with the TNF-α inhibitor C87 (Ma et al., 2014) abolished the increase in firing frequency (both p > 0.5) (Figure 3C). To confirm the effect of TNF-α, neurons were subjected to bath application of TNF-α, and the TNF-α treatment increased firing frequency similar to that observed following LPS administration (*p < 0.03) (TNF-α, Figure 3D). Pre-exposure to TNF-α prevented the firing increase in response to LPS application (p > 0.5) (LPS after TNF-α, Figure 3D), implying that TNF-α release and excitability plasticity resulted from LPS application. Although our results suggest that TNF-α directs Purkinje neurons to enhance excitability, the mechanisms underlying this process remain unclear. A series of studies in hippocampal neurons previously demonstrated that TNF-α activates phosphatase signaling via TNF receptor 1 in CA1 pyramidal neurons (Beattie et al., 2002; Pribiag and Stellwagen, 2013). Then, we subjected Purkinje neurons to bath application of TNF-α under suppression of phosphatase activity by intraneuronal okadaic acid, but there were no increases in firing frequency (p > 0.3) (Figure 3E), suggesting the TNF-α-mediated firing plasticity occurred through phosphatase activity.

We also monitored action potential firing in the presence of protein-synthesis inhibitors anisomycin and cycloheximide,

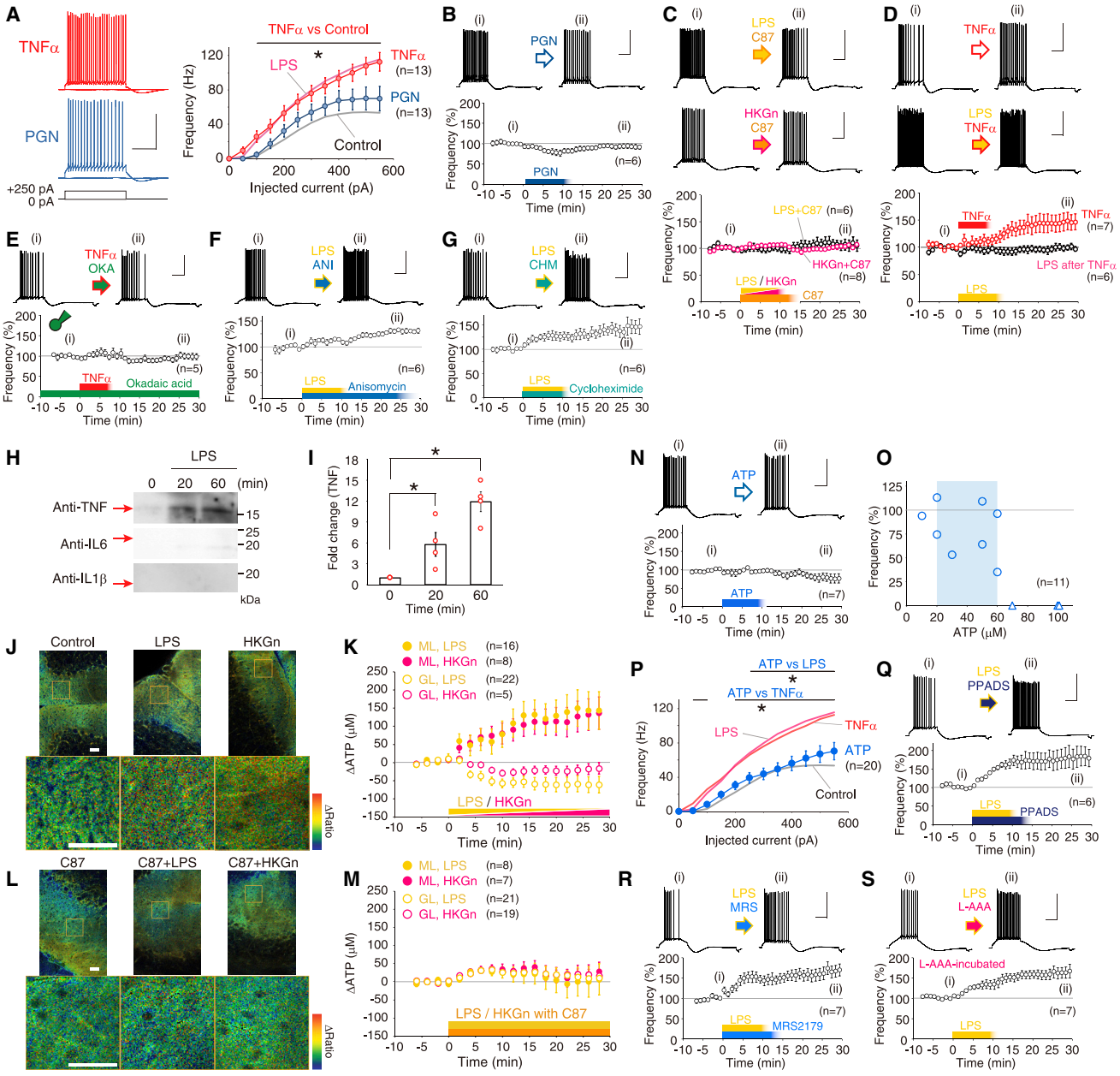

Figure 3. Involvement of Microglial Mediators in the Increase of Neuronal Excitability

(A) Firing frequency of Purkinje neurons exposed to TNF-α (100 ng/mL) and peptidoglycan (PGN) (10 μg/mL) against depolarization pulses. *$p < 0.03$. Mean firing frequencies of neurons exposed to lipopolysaccharide (LPS) and control neurons are merged for comparison.

(B) PGN exposure. Representative firing, before (i) and after (ii) exposure, and time courses are shown. Reagent application began at 0 min and continued for 7–10 min.

(C) Suppression of firing plasticity induced by LPS- and heat-killed Gram-negative bacteria mixture (HKGn) by TNF-α inhibitor C87 (40 μM).

(D) TNF-α bath application increased the firing frequency and occluded the effect of LPS.

(E) TNF-α-induced firing frequency increase was abolished by intraneuronal okadaic acid (150 nM).

(F and G) Action potential firing following LPS exposure under treatment with anisomycin (30 μM, F) and cycloheximide (30 μM, G). Although the data suggested that the firing increase by exposure to LPS was induced under suppression of protein translation, a minor and insignificant reduction of the extent of increase in firing frequency was noticed compared with LPS-conditioned experiments shown in Figure 1B.

(H) Western blotting of TNF, IL-6, and IL-1β protein in supernatant following LPS exposure for 0, 20, and 60 min.

(I) Fold change in TNF level normalized by at 0 min.

(J) FRET imaging with the ATP probe GO-ATeam2 shows the increase in ATP in cerebellar slices of GO-ATeam2 transgenic mice (J–M).

(K) Time courses of changes in ATP concentration in the molecular layer (ML) and granule cell layer (GL). See also Figure S3.

(legend continued on next page)

which did not prevent LPS-induced firing increases (*p < 0.03 for both) (Figures 3F and 3G). Western blotting confirmed the increase in the amount of TNF-α, but not IL-6 or IL-1β (Figures 3H and 3I), by transient exposure to LPS, indicating that TNF-α release mediates signaling between microglia and Purkinje neurons. These findings suggest that endotoxin exposure may stimulate TNF-α secretion from microglia in a protein-synthesis-independent manner and that diffusible TNF-α triggered the increase in neuronal excitability.

It is also possible that bacterial endotoxin triggers excitability plasticity via ATP release from tissues including microglia (Aguzzi et al., 2013; Yirmiya et al., 2015; Pascual et al., 2012; Kettenmann et al., 2011). Hence, we investigated ATP synthesis and release in the whole cerebellum in knockin mice with the ATeam probe GO-ATeam2 (see STAR Methods) and applied them in a new way. Two-photon fluorescence or Förster resonance energy transfer (FRET) imaging suggested that continuous exposure to both LPS and heat-killed Gram-negative bacteria increases ATP concentration prominently in the cerebellar molecular layer (Figures 3J, 3K, and S3A). Cell-level images also suggest that the increase in ATP does not occur in interneurons in the molecular layer, Purkinje cell bodies and dendrites, granule cells, interneurons in the granule cell layer, or bundles in the white matter (Figures S3B–S3G). We estimated the changes in ATP concentration from the FRET ratio changes against endotoxin exposure (see STAR Methods), and the extent of ATP increase reached 140 μM in the molecular layer (Figure 3K). Increase in ATP was prevented under TNF-α inhibition by C87 (Figures 3L and 3M), suggesting the ATP synthesis follows TNF-α secretion. Next, we tested whether bath application of ATP with various concentrations (10–100 μM) modulates the excitability of Purkinje neurons (Figures 3N–3P). The firing frequency did not increase upon exposure to ATP (20–60 μM, p > 0.1) (Figures 3N and 3P). Neurons in the CNS respond to ATP via a broad subfamily of purinergic type 2 receptors (P2Rs). Tzour et al. (2017) reported that the activation of astrocytic P2Y1 receptors is important for the increase in excitability of pyramidal neurons during LPS exposure in the hippocampal slices. Here, we monitored the firing frequency in the cerebellar Purkinje cells under the P2R inhibitor PPADS and more specific inhibitor of P2Y1 receptors MRS2179, but both firing frequencies increased upon exposure to LPS (PPADS, *p < 0.05; MRS2179, *p < 0.002) (Figure 3Q and 3R). Finally, we monitored LPS-triggered firing plasticity under suppression of astrocytes using gliotoxin L-2-aminoadipic acid (L-AAA), but the firing increases were not impaired (*p < 0.003) (Figure 3S), suggesting astrocytes were not involved in the firing increase.

Facilitation of Synaptic Transmission following Microglial Activation

Regarding the effect of endotoxin exposure in synapses, we first examined whether LPS administration alters spontaneous excitatory postsynaptic currents (sEPSCs). Results suggested less change in sEPSC amplitude in Purkinje neurons, except for a minor reduction in the PPADS+LPS group (Figures 4A–4D). Meanwhile, administration of LPS, TNF-α, heat-killed Gram-negative bacteria, and ATP produced a significant increase in sEPSC frequency (Figures 4E and 4F). Our findings suggest that activated microglia promoted vesicular release from presynaptic neurons, depending on both TNF-α and ATP. Extracellular ATP may increase in vesicular release via purinergic receptors on presynaptic neurons. In microglia-depleted cerebella, there were no significant differences among microglia-depleted control, LPS, and heat-killed Gram-negative bacteria exposure groups in amplitude or in frequency, indicating the involvement of certain mediators from microglia (Figures 4G–4I). However, the analysis of sEPSCs includes changes in the activity of presynaptic neurons. To avoid such an effect, we monitored miniature excitatory postsynaptic currents (mEPSCs) under suppression of neuronal activity by tetrodotoxin (TTX). Results of the analysis showed increases in both mEPSC amplitude (Figures 4J–4M) and mEPSC frequency (Figures 4N and 4O) after administration of LPS, TNF-α, heat-killed Gram-negative bacteria, and ATP. These results suggest potentiation of both postsynaptic responsiveness and presynaptic release after exposure to endotoxin and microglial activation, at least through purinergic receptors.

Endotoxin-TLR4-TNF-α Signal Involvement in Hyperexcitability

Next, we investigated whether the endotoxin receptors are involved in microglia-associated signaling. LPS is classically known to bind complement receptor 3 in immune cells (Kettenmann et al., 2011; Pandey et al., 2014). Zhang et al. (2014) revealed that application of LPS under hypoxic conditions resulted in the release of superoxide anion via complement receptor and nicotinamide adenine dinucleotide phosphate (NADPH) oxidase activity. Here, we applied LPS in the presence of apocynin, an NADPH oxidase inhibitor. However, we observed no suppression of firing increases (*p < 0.03) (Figure 5A), implying that neither the superoxide nor the complement receptor pathway is involved in the induction of this excitability plasticity.

The Toll-like receptor (TLR) family comprises pattern recognition receptors that are abundantly expressed on the surface of immune cells. The extracellular domain of leucine-rich repeats of TLR4 specifically recognizes LPS (Park et al., 2009), and its dimerized complex is thought to trigger the intracellular signaling

(L and M) FRET ATP imaging under TNF-α blocker C87 (40 μM). The FRET images under inhibition of TNF-α (L) and normalized time courses (M) of changes in ATP concentration in ML and GL are shown. The ATP increase in the molecular layer by endotoxin LPS and HKGn was abolished by TNF-α inhibition.
(N) 20–60 μM ATP exposure.
(O) Firing changes after exposure to ATP in various concentrations. Each dot indicates the mean firing change after 25 to 30 min. Purkinje cells ceased firing with exposure to a high ATP concentration (>60 μM, n = 3, triangles).
(P) Firing frequency after ATP administration (20–60 μM). The firing frequency in response to depolarization pulses is shown. *p < 0.05, two-tailed Mann-Whitney U test.
(Q and R) LPS exposure in the presence of PPADS (50 μM, Q) and MRS2179 (30 μM, R), suggesting that firing increase was not abolished by P2X and P2Y receptor inhibitors, respectively.
(S) LPS exposure under suppression of astrocyte activity. Recordings were done in the cerebellar slices incubated with L-AAA (1 mM, 1–2 h) beforehand.
Data are represented as mean ± SEM. All right-angle scales: 40 mV and 200 ms. Bar scales: 50 μm (J and L). See also Table S1.

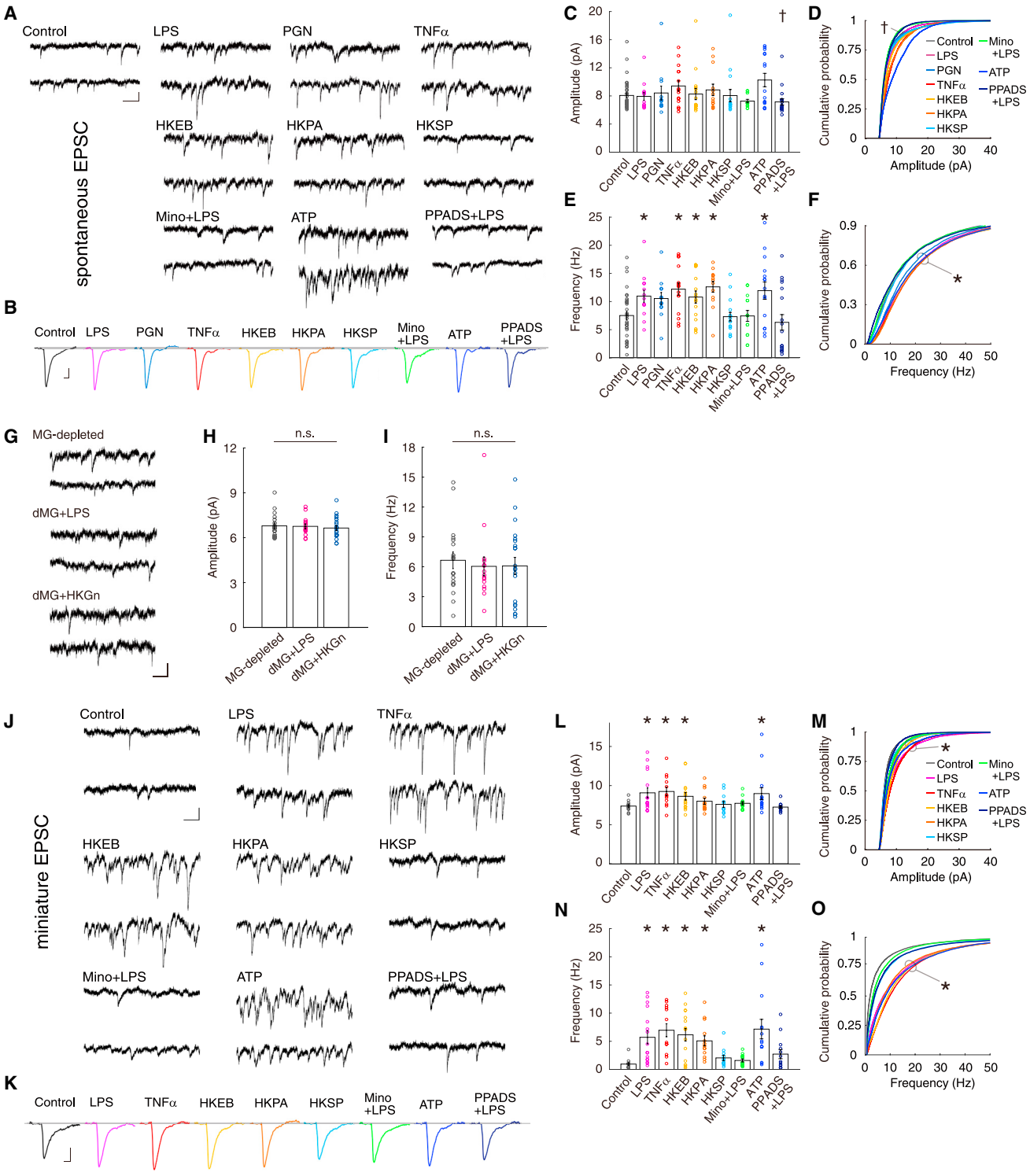

Figure 4. Increase in the Release of Excitatory Synaptic Transmissions following Microglia Activation in Both a TNF-α- and an ATP-Dependent Manner

(A) Spontaneous excitatory postsynaptic currents (sEPSCs) of rats in control, lipopolysaccharide (LPS), peptidoglycan (PGN), TNF-α, heat-killed *Escherichia coli* 0111:B4 (HKEB), heat-killed *Pseudomonas aeruginosa* (HKPA), heat-killed *Streptococcus pneumoniae* (HKSP), minocycline+LPS, ATP, and PPADS+LPS. Scale: 10 pA and 100 ms.

(B) Averaged representative sEPSCs. Scale: 2 pA and 10 ms.

(legend continued on next page)

cascade. We examined microglia signaling using pharmacology and transgenic animals. Under the inhibition of TLR4 by C34 (Neal et al., 2013), LPS exposure did not cause a change in firing frequency ($p > 0.1$) (Figure 5B). Exposure of TLR4-knockout cerebellar slices to LPS and heat-killed Gram-negative bacteria abolished the induction of the firing increase (Figures 5C and 5D), whereas Purkinje neurons in TLR2-knockout mice showed an increase in firing sustainably (Figure 5E), suggesting that TLR4, but not TLR2, is essential for the observed responses (Figures S4A and S4B). We next aimed to determine the downstream of TLR4 using knockout mice for myeloid differentiation primary response gene 88 (MyD88) and Toll/IL-1 receptor (TIR) domain-containing, adaptor-inducing interferon-β (TRIF). MyD88 is a TIR domain-containing adaptor common in TLR signaling pathways, and TRIF mediates the MyD88-independent pathway downstream of TLR3 and TLR4 (Pandey et al., 2014). Both are involved with the release of inflammatory cytokine in macrophages and microglia. In MyD88- and TRIF-knockout mice, no significant difference was observed in firing frequency between LPS-treated and untreated neurons (Figures S4C and S4D) or in firing properties (Table S2). In addition, LPS exposure did not produce long-lasting firing increases (both, $p > 0.7$) (Figures 5F and 5G), suggesting that both pathways in microglia are necessary for the induction of excitability plasticity. In microglia, the precise machinery underlying the exocytosis of inflammatory cytokines remains obscure; however, a certain molecule downstream of both signals may prime the secretion of soluble TNF-α, as illustrated in a summary cascade of the endotoxin-induced excitability plasticity in the cerebellum (Figures 5H–5J and S4E).

Depressive Behaviors of Animals with Cerebellar Inflammation

To reveal the physiological significance of excess immune activity in the cerebellum in living animals, we observed animals' behavior after bacterial endotoxin infusion in anterior lobes of the cerebellar vermis. Unexpectedly, we found that the spatial exploratory behavior of freely moving rats in an open field was significantly reduced by administration of LPS (1 mg/mL) and heat-killed Gram-negative bacteria (HKEB+HKPA, 10^9 cells/mL for each) (Figures 6A and 6B; Video S1). In a social interaction test, LPS- and heat-killed Gram-negative bacteria-injected rats exhibited considerably less interest in siblings (Figure 6C). Immobility time during a forced swim test became significantly elongated compared with that in control PBS-injected animals (Figure 6D). These results suggest that animals with cerebellar injection of inflammatory substances exhibit depression-like or abulic behavior, in contrast to autistic behaviors in animals with less excitable Purkinje neurons (Tsai et al., 2012; Stoodley et al., 2017). To examine the extent of repetitive movements, we conducted a marble-burying test and found that rats with cerebellar bacterial endotoxin infusion showed less burying behavior (Figures 6E and 6F). Animals with cerebellar injection did not show significant motor discoordination or ataxia (Figures S5A and S5B), even with a high density of LPS (20 mg/mL, 0.30 μL, n = 5, data not shown). These results of the behavior battery test suggest depression-like phenotypes of the acute inflammation of the anterior lobes.

Then, we estimated the extent of the inflammation in space and time. How much cerebellar space does the acute inflammation fill, over how much area does the reagent spread, and how long does the hyperexcitability continue? To image the region of inflammation *in vivo*, we used a fluid attenuation inversion recovery (FLAIR) sequence of magnetic resonance (MR) imaging. MR FLAIR images clearly showed inflammation at the restricted position of the heat-killed Gram-negative bacteria injection (Figure 6G) (see STAR Methods). Postinjection histology clarified the localized spread of the reagent (Figure S5G). Purkinje neuron activity following the drug injection showed a significant increase in the firing frequency of neurons *ex vivo* from LPS- and heat-killed Gram-negative bacteria-injected cerebella for ~6 h (Figures S5C and S5D). The behavioral modulation and high excitability of neurons lasted only until the following day (Figure S5E and S5F). Altogether, transient hyperexcitability in the cerebellum through region-specific inflammation caused a reduction of psychomotor activity.

Recovery of Behavioral Disturbances by Immune Suppression

Provided that activated microglia secrete molecules during inflammation *in vivo*, microinfusion of such molecules may suffice to modulate animal behavior. We next applied TNF-α (20 μg/mL) and ATP (20 mM) in the cerebellar anterior lobes and found that TNF-α, but not ATP, reduced behaviors (Figures S6A–S6F). This result indicates that suppression of TNF-α

(C–F) Bar graphs (mean ± SEM) and cumulative probability graphs of amplitude (C and D) and frequency (E and F) of sEPSCs in different experiments, respectively. A total of 35, 13, 12, 15, 16, 13, 16, 14, 15, and 18 cells were observed. Asterisks indicate a significance increase (multiple comparison with Kruskal-Wallis test) against the control condition, and a dagger indicates a decrease. LPS, Gram-negative bacteria, TNF-α, and ATP increased sEPSC frequency. Suppression of the increase in sEPSC frequency by PPADS suggests the involvement of P2 receptors.

(G) Representative sEPSC traces of microglia-depleted mice. Scale: 10 pA and 100 ms.

(H and I) Bar graphs of amplitude (H) and frequency (I) of sEPSC in different experiments (mean ± SEM) are shown. Total numbers of 18, 15, and 21 cells were recorded in the microglia-depleted (dMG) control, dMG+LPS, and heat-killed Gram-negative bacteria mixture (HKGn) exposure, respectively. Microglia-depleted C57BL/6J mice were used in the experiments (G–I). No significant differences (n.s.) were observed among all pairs for both amplitude and frequency ($p > 0.3$, multiple comparison), as well as rise time, half-width, and decay time (data not shown).

(J) Miniature excitatory postsynaptic currents (mEPSCs) of rats in control, LPS, TNF-α, HKEB, HKPA, HKSP, minocycline+LPS, ATP, and PPADS+LPS. Scale: 10 pA and 100 ms.

(K) Averaged representative mEPSCs. Scale: 2 pA and 10 ms.

(L–O) Bar graphs (mean ± SEM) and cumulative probability graphs of amplitude (L and M) and frequency (N and O) of mEPSC in different experiments, respectively. A total of 13, 16, 13, 16, 13, 12, 14, 14, and 13 cells were observed. Asterisks indicate a significance increase (multiple comparison) against the control. LPS, Gram-negative bacteria, TNF-α, and ATP increased in both amplitude and frequency. Suppression of the increase in mEPSC frequency by PPADS suggests the involvement of P2 receptors.

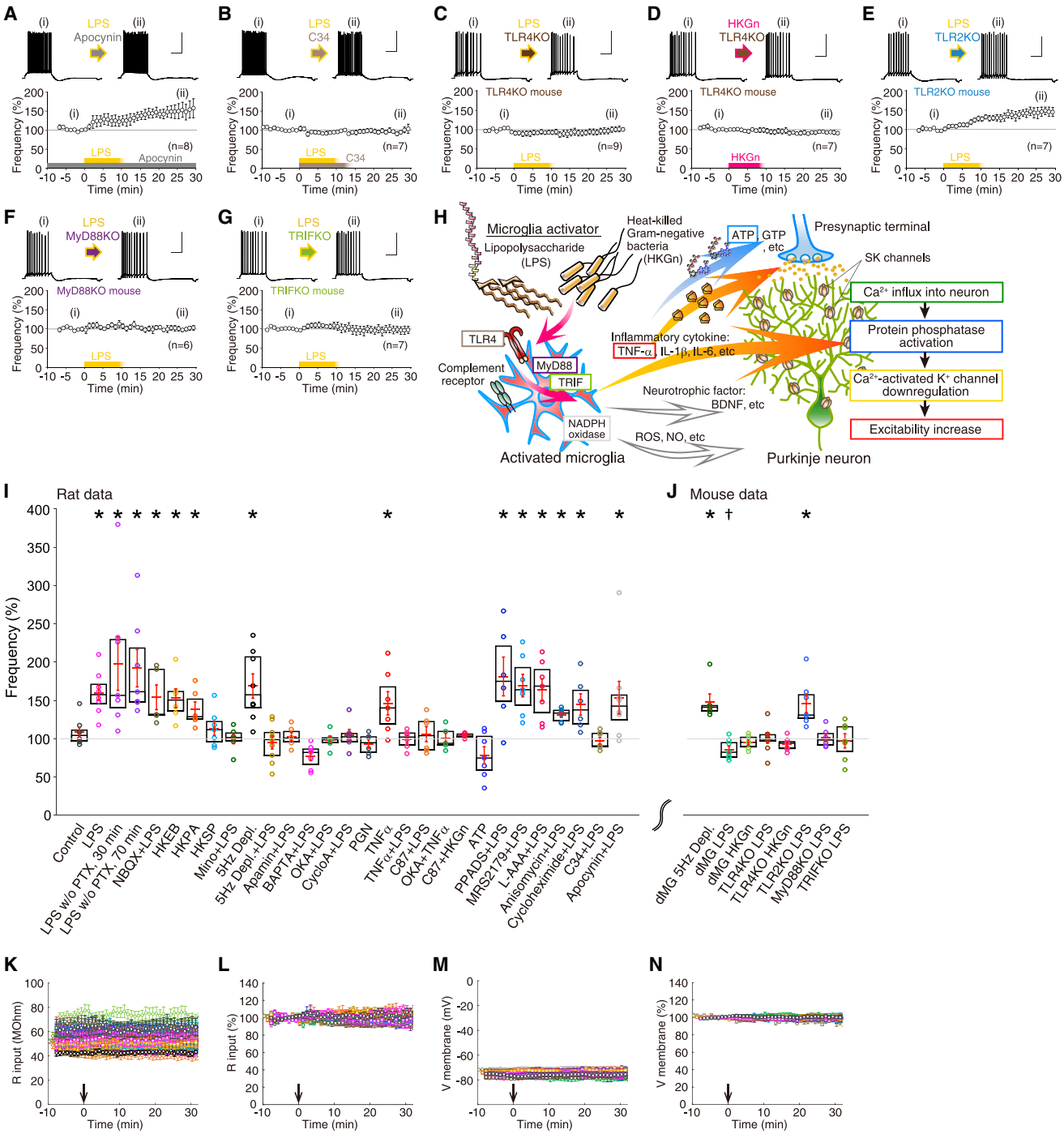

Figure 5. Endotoxin-TLR4-TNF-α Signal Involvement of Excitability-Increased Plasticity by Microglia Activation

(A) Firing increase by lipopolysaccharide (LPS) under a nicotinamide adenine dinucleotide phosphate (NADPH) oxidase inhibitor, apocynin (100 μM).

(B) LPS-induced firing increase plasticity was abolished by Toll-like receptor 4 (TLR4) blocker C34 (40 μM).

(C–E) Impairment of the excitability plasticity in TLR4-knockout (KO) mice (C and D), but not in TLR2-KO mice (E). The LPS (C and E) or heat-killed Gram-negative bacteria mixture (HKGn) (D) was exposed.

(F and G) Impairment of the excitability plasticity in transgenic mice lacking the TLR4 downstream proteins MyD88 (F) and TRIF (G). Reagent application began at 0 min and continued for 10 min. Data are represented as mean ± SEM. Scales: 40 mV and 200 ms.

(H) Summary of the signaling cascade.

(I and J) Summary of the extent of excitability changes. Firing frequency changes after the application of various reagents or conditioning for intrinsic plasticity in rat neurons (I) and mouse neurons (J). All data from long-term recordings in this study were summarized as mean ± SEM (red mark) with a boxplot. Averaged firing

(legend continued on next page)

should help reduce the animals' depression-like behaviors. Co-injections of heat-killed Gram-negative bacteria with C87 (2–4 mM) into the anterior lobes of the cerebellar vermis showed recovery from the impairment of psychomotor behaviors (Figures 6A–6F and Video S1, HKGn+C87; Figures S6G–S6K, controls of C87), as well as inflammation (Figure 6G, HKGn+C87) and neuronal excitability (Figures S5C and S5D, HKGn+C87). We speculated that the microglia depletion may also cancel the psychomotor depressiveness by endotoxin, and the results obtained in Ki20227-administered animals proved that this was the case (Figures 6A–6F, dMG+LPS; Figures S6G–S6K, controls of microglia depletion). Altogether, these striking effects of endotoxin infusion were substantially rescued by both co-injection with TNF-α inhibitor and microglia depletion (Figure S6L).

However, the causality between abnormal behaviors and cerebellar hyperexcitability resulting from acute inflammation is elusive. Next, we conducted functional MR imaging (fMRI) of resting-state animals to investigate which regions of brain activity are related to the activity of cerebellar anterior lobes (see STAR Methods). The resting-state (rs) fMRI showed distinct enhancement of correlated signals among the heat-killed Gram-negative bacteria-infused cerebellar anterior vermis and frontal neocortical areas, including the medial prefrontal cortex (mPf), cingulate cortex (Cg), and primary motor cortex (M1) (Figures 6H–6J and S7). In addition, TNF-α inhibitions rescued the functional overconnectivity caused by cerebellar inflammation (i.e., hyperexcitation in the cerebellar cortex) (Figures 6H and 6I, HKGn+C87), suggesting that modulation of long-range connectivity between the cerebellar vermis and the prefrontal areas may relate to the animals' behavioral modulations.

Region-Specific Inflammation Modulates Animal Behavior in Distinct Manners

In autistic-model animals in previous studies, activity in the simple lobule, including crus II, was shown to relate behavioral abnormality (Stoodley et al., 2017; Tsai et al., 2018). Therefore, we investigated the regional dependence of behavioral modulation in our cerebellar inflammation model. In addition, we injected LPS into different regions of the cerebellum (Figure 7). Although infusion into the posterior vermis did not show significant changes in animals' behaviors, infusion into the right hemisphere induced obsessive behaviors, which increased in marble-burying and same-corner-preference scores (Figures 7D and 7F). Results from the sniffing test also suggest inflammation in the anterior vermis and hemisphere depressed animal behaviors (Figure 7G). A summary table of behavior modulation against acute inflammation in the distinct cerebellar regions suggests the different phenotypes as depression- and autistic-like behaviors (Figure 7H).

DISCUSSION

The results of the present study indicate that activated microglia elicit the induction of long-term potentiation (LTP) of intrinsic excitability, facilitate synaptic transmission in cerebellar Purkinje neurons, and modulate psychomotor behaviors. The excitability plasticity of the cerebellar Purkinje neurons is considered mediated by M1 microglia. Macrophages secrete TNF-α rapidly upon their activation through a non-constitutive pathway (Murray et al., 2005). Thus, the mediator release in a relatively rapid timescale from activated microglia may explain the time course of increased firing against exposure to LPS or heat-killed Gram-negative bacteria (Figures 1D and 1G) and the translation independency of plasticity induction (Figures 3F and 3G). Our results of the increase in TNF-α release, at least within 20 min of western blotting, support this notion (Figures 3H and 3I). On the other hand, previous studies have shown that glial TNF-α signaling induces trafficking of ionotropic receptors at synapses (Beattie et al., 2002; Pribiag and Stellwagen, 2013). These trafficking mechanisms of ion-channel receptors underlie PP activity. Our results of cerebellar microglia-neuron interaction via TNF-α also suggest the involvement of phosphatase activation for SK-channel downregulation following TNF receptors in neurons (Figure 3E), although there is a possibility of the involvement of multiple ion channels: BK, A-type voltage-gated K^+ channels, and hyperpolarization-activated cyclic nucleotide-gated (HCN) channels. TNF-α does not solely target the neuronal membrane; secreted TNF-α is also known to modulate presynaptic transmission via TNF receptors on astrocytes (Santello et al., 2011; Habbas et al., 2015). Bergmann glia, a type of astrocyte in the cerebellum, may promote presynaptic release following TNF-α stimulation. Our finding regarding the increase in s/mEPSC frequency (Figures 4E and 4N, TNF-α) is consistent with this scenario, but it is beyond our scope to address it further.

ATP is a gliotransmitter released from neocortical and hippocampal astrocytes upon their Ca^{2+} activity (Zhang et al., 2007; Lalo et al., 2014). Astrocytic ATP in the mPf mediates antidepressant effects through P2X receptors (Cao et al., 2013). Although several types of cells are located in the cerebellum, no precisely imaged data regarding the ATP source had been presented. Our imaging with the new ATP probe (Figures 3J–3M) visualized that the ATP concentration was increased during exposure to endotoxin in the molecular layer of the cerebellar cortex, but not in the granule cell layer, suggesting the distinct source of ATP in the cerebellum. Cell-level images with high resolution also suggest that the ATP increase occurs insubstantially in neurons in both layers and bundles in the white matter (Figures S3B–S3G). In addition, pharmacological TNF inhibition substantially prevented such ATP increase, which suggests TNF-α secretion from microglia is a trigger for ATP synthesis or its amplification in the molecular layer (Figures 3L and 3M). Altogether, the major ATP source

changes at 25 to 30 min or at 65 to 70 min were collected. Asterisks indicate significant increases against the baseline (*$p < 0.05$, multiple comparison with Kruskal-Wallis test). A dagger indicates a significant decrease (†$p < 0.05$).
(K and L) Input resistance (K) and its normalized values (L) of the experiments of intrinsic plasticity. An arrow at 0 min indicates the start of the application of endotoxin, reagents, and conditioning. The change in input resistance was normalized between −5 and −1 min. All color codes follow those in (I) and (J).
(M and N) Membrane voltage (M) and its normalized values (N) of the experiments.
See also Figure S4 and Table S2.

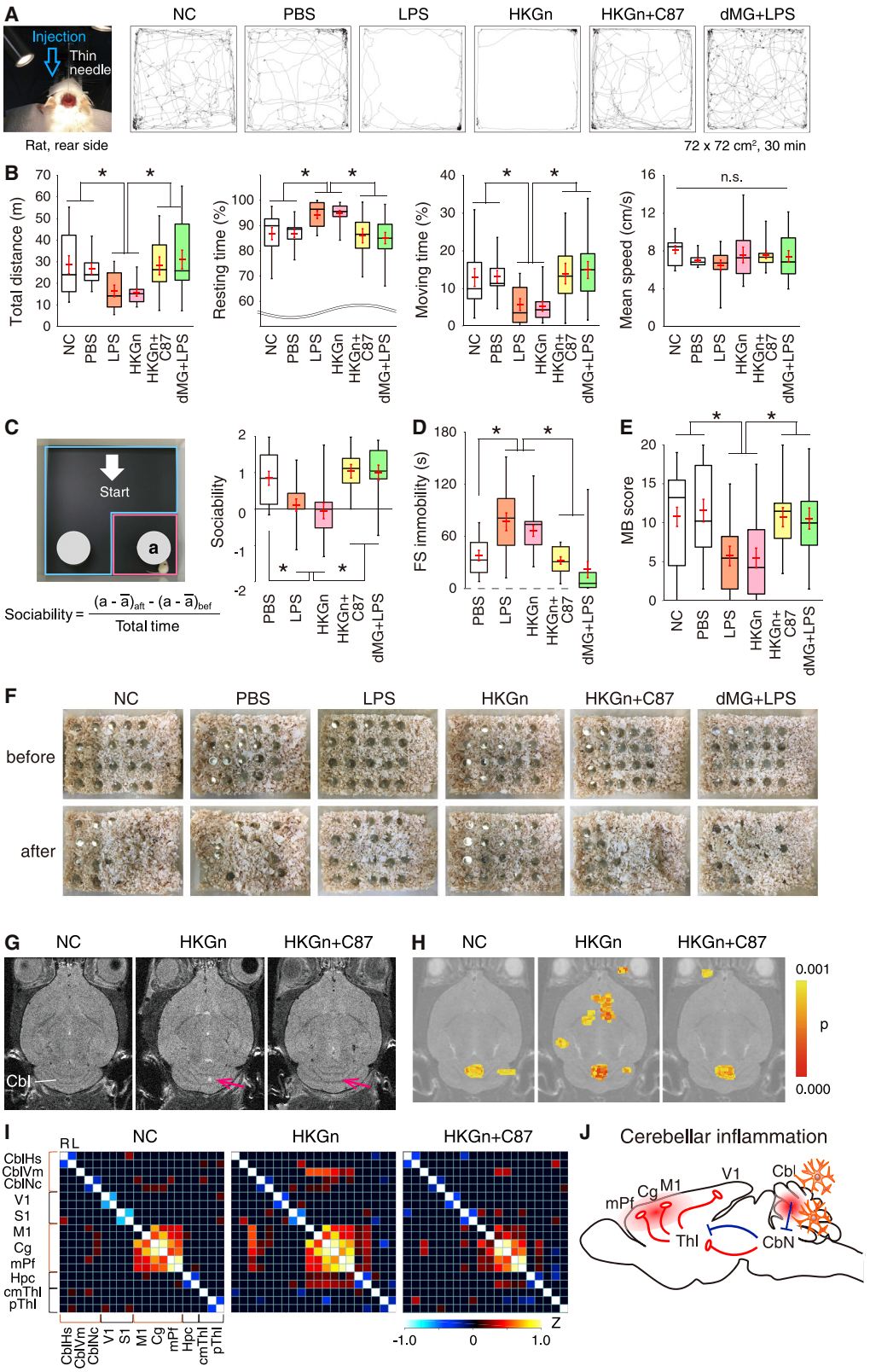

(legend on next page)

in response to immunotriggering is suggested to be Bergman glia or other cells in the molecular layer.

In response to LPS administration, ATP has been shown to facilitate presynaptic release through P2Y receptors in the hippocampal slices (Pascual et al., 2012) without TNF-α involvement, which is in agreement with our result of the increase in s/mEPSC frequency by sole ATP administration (Figures 4E, 4F, 4N, and 4O, ATP). Meanwhile, in the cerebellum, ATP acts as a diffusible trigger of Ca^{2+} waves through P2Rs in Bergman glial processes (Hoogland et al., 2009). It was shown that such Bergmann glial Ca^{2+} activity does not modulate presynaptic release from the glutamatergic excitatory terminals, at least on a short timescale (Beierlein and Regehr, 2006). Therefore, ATP-induced Ca^{2+} activity in Bergmann glia and following astrocytic Ca^{2+}-dependent messengers may not relate to the increase in s/mEPSC, although the exact mechanism remains unsolved (Figures 4F and 4O, PPADS+LPS).

Activated microglia release not only TNF-α and purines (ATP and guanosine triphosphate [GTP]) but also other inflammatory cytokines (IL-1β and IL-6), trophic factors (brain-derived neurotrophic factor), and reactive oxygen species (ROS) (e.g., superoxide and nitric oxide) (Parkhurst et al., 2013; Prinz and Priller, 2017; Pascual et al., 2012; Zhang et al., 2014; Kettenmann et al., 2011). Our electrophysiological experiments suggest that ATP and ROS were not involved in the induction of intrinsic excitability increase (Figures 3N and 5A). Rather, considering the reduction of firing frequency at high ATP concentrations, cerebellar microglia could regulate neuronal excitability in a bimodal direction through TNF-α and ATP (Yirmiya et al., 2015) in a local region. Other inflammatory cytokines are possibly involved; IL-1β has been shown to prevent LTP induction of population spikes in the hippocampal CA1 (Bellinger et al., 1993), although inhibition of IL-1β prevents its maintenance (Schneider et al., 1998). Microglia-specific transcriptomic data suggest changes in the gene profile after lesion (Tay et al., 2017); thus, modulation of neuronal activity might be up to the history of tissue microglia. The relevance of this phenomenon to the late phase of intrinsic plasticity has not yet been investigated, but our western blotting suggests that the protein level of both IL-1β and IL-6 was scarce to detect in response to acute exposure to LPS in the cerebellum (Figure 3I). Otherwise, TNF-α can have consequences on enzymes other than okadaic acid-sensitive phosphatases, which in turn likely have more substrates than only SK channels.

The cerebellum is the principal regulator of motor coordination, timing, and adaptation (Ito, 2008; De Zeeuw and Ten Brinke, 2015; Boyden et al., 2004; Inoshita and Hirano, 2018). The vestibular cerebellum had been linked to eye movements and reflections, whereas the anterior vermis of the cerebellum had been thought to relate to autonomic nervous system (Reis et al., 1973; Supple and Kapp, 1993). Although our acute inflammation model did not show severe motor deficits (Figures S5A and S5B), 20-μM apamin-injected rats showed ataxia (4 rats of 5 tested animals, data not shown), suggesting the inflammatory effects do not achieve full suppression of SK channels in the injected region during inflammation. We do not intend to claim the cerebellum is no longer involved in motor control and coordination but is potentially involved in psychomotor behaviors. Results of hyperexcitability of the Purkinje cells and increases in synaptic transmission in the anterior lobes may suppress the activity in the fastigial nucleus transiently and produce behavioral depressiveness (Figures 6A–6F). In Brown and Raman (2018), optogenetical activation of the Purkinje neurons in crus I/II and the resultant suppression in the dentate CbNs decreased the instant whisker movements. These results may suggest a difference of biological significance for distinct behaviors among CbN. Researchers have started targeting its cognitive functions, and clinical studies have been suggesting involvement of the cerebellum in psychiatric disorders, potentially via dysmetria of thought, manifested by autism spectrum disorders, dyslexia, and schizophrenia (Schmahmann, 2004; Tsai et al., 2012, 2018; Piochon et al., 2014; Koziol et al., 2014; Witter and De Zeeuw, 2015; Stoodley et al., 2017). Akinetic mutism or abulia are also frequently observed after surgical operation of cerebellar astrocytoma or medulloblastoma (Robertson et al., 2006), implying the disruption of connections in regions responsible to speech and motivation through the cerebellar vermis during postoperative inflammation. Histological studies have proved anatomical connection between the cerebellum and the neocortex (Kelly

Figure 6. Induction and Rescue of Psychomotor Depressiveness Attributed from Cerebello-frontal Functional Overconnectivity

(A) Representative trajectories of exploration behavior of drug-infused rats in the open field arena. PBS, lipopolysaccharide (LPS), heat-killed Gram-negative bacteria mixture (HKGn), HKGn+C87, LPS to microglia-depleted animals (dMG+LPS), or nothing (non-conditioned [NC]) was injected into the anterior cerebellar vermis.

(B) Boxplots of the total distance, resting time, moving time, and mean speed. Whiskers of boxes show the entire range of data. Overlapping red marks represent mean ± SEM. *$p < 0.05$, multiple comparison. Co-injection of TNF-α inhibitor C87 and microglia deletion significantly reduced the sluggishness of animals.

(C) Social interaction.

(D) Forced swim test.

(E) Marble-burying score.

(F) Pictures of marble-burying behavior before and after 20 min of monitoring of drug-infused rats. PBS, LPS, HKGn, HKGn+C87, dMG+LPS, or nothing (NC) was injected into the cerebellar vermis. Rats with LPS and HKGn injection hid fewer marbles compared with those with NC, PBS, HKGn+C87, and dMG+LPS.

(G) FLAIR magnetic resonance images indicate inflammation in HKGn, but not in HKGn+C87. In FLAIR images, the high signal intensity is depicted in white. Magenta arrows indicate the locations of injection.

(H) Resting-state functional magnetic resonance imaging (rs-fMRI) of control and HKGn- and HKGn+C87-infused rats. A seed was given in the anterior lobe of cerebellar vermis. Color coding indicates the functional connectivity obtained from the blood-oxygen-level-dependent (BOLD) signal.

(I) Seed-seed correlation maps shown with *Z* score. Seeds were applied in the right and left hemispheres, marked by R and L, respectively, except for the anterior lobe of the cerebellar vermis (CblVm) and centro-medial thalamus (cmThl). The correlation is enhanced in HKGn between CblVm and M1+Cg+mPf (i.e., primary motor cortex + cingulate cortex + medial prefrontal cortex). Abbreviations of brain regions are described in STAR Methods.

(J) Schematic drawing of activated regions during cerebellar inflammation.

See also Figures S5–S7.

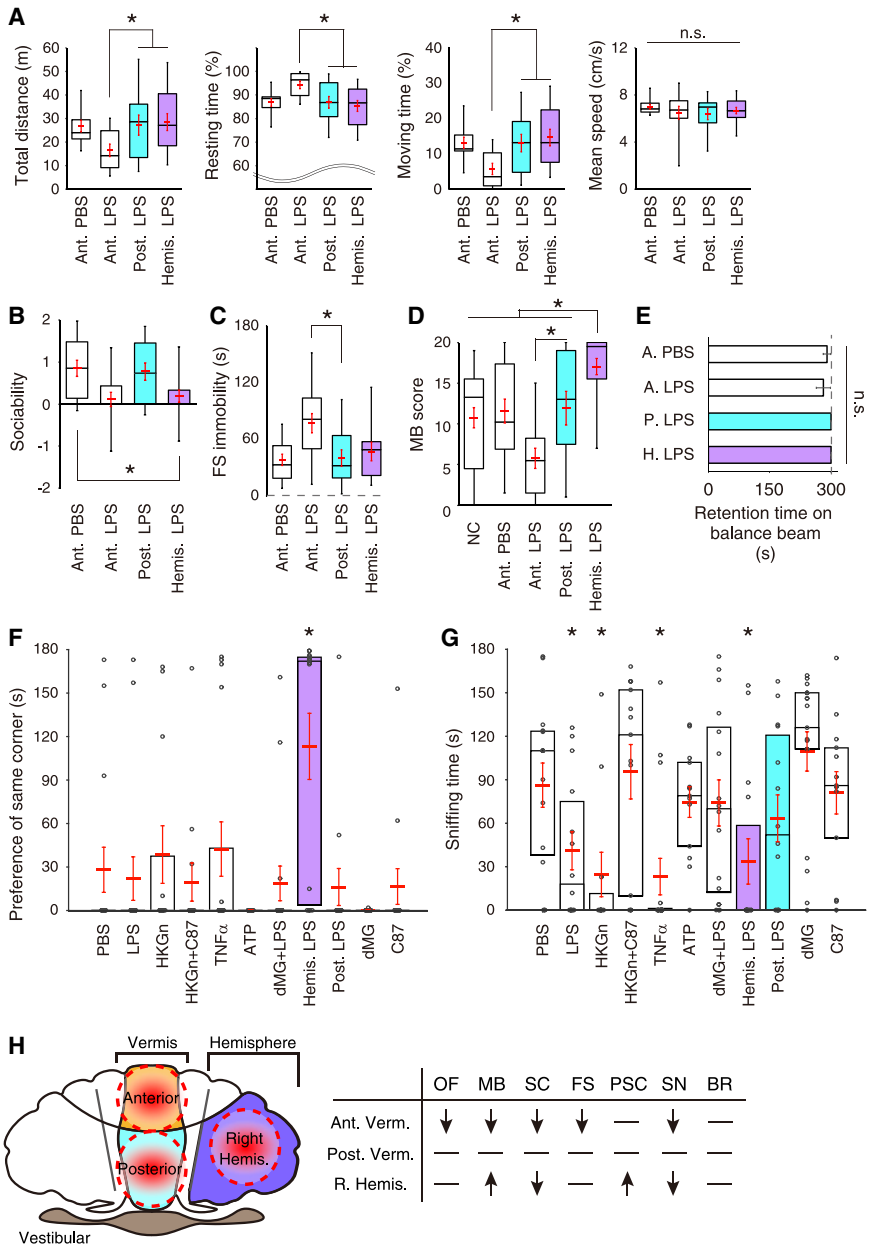

Figure 7. Region-Specific Inflammation Modulates Animal Behavior in Distinct Ways

(A) Boxplots of total distance, resting time, moving time, and mean speed of exploration behavior of drug-infused rats in the open field arena. Whiskers of boxes show the entire range of data. Overlapping red marks represent mean ± SEM. Lipopolysaccharide (LPS) was injected into the anterior cerebellar vermis (Ant.), posterior cerebellar vermis (Post.), or right hemisphere (Hemis.).

(B) Social interaction.

(C) Forced swim test.

(D) Marble-burying score. Results of NC (non-conditioned), PBS, and LPS in the anterior vermis of Figures 6B–6E are for comparison. Overlapping red marks represent mean ± SEM. *p < 0.05, multiple comparison. * between Ant. LPS and Ant. PBS or NC were omitted because of redundancy.

(E) Posture retention test on a balance beam. Results of PBS and LPS injected into the anterior vermis of Figure S5A are for comparison.

(F) Time spent in the corner the rats preferred previously. Red marks represent mean ± SEM. Boxplots with all data points are overlaid. Animals with LPS injection into the right hemisphere show strong obsession, while those injected to the left hemisphere did not (data not shown). *p < 0.05, multiple comparison (versus PBS).

(G) Sniffing time. *p < 0.05, multiple comparison (versus PBS).

(H) Summary of behavioral changes. Arrows indicate the direction of behavioral changes with significant differences by multiple comparison. OF, open field test; MB, marble-burying test; SC, sociability test; FS, forced swim test; PSC, preference of the same corner; SN, sniffing test; BR, retention test on balance bar.

and Strick, 2003; Suzuki et al., 2012). Such connections may contribute to a range of cognitive functions (e.g., dyslexia, stuttering disfluency, and depressiveness). Here, our results clarify not only the mechanism of microglia-induced hyperexcitability in the cerebellar circuit but also the psychomotor depressiveness resulting from functional overconnectivity in cerebello-frontal projections (Figures 6I and 6J). Given that Purkinje cells are inhibitory and tend to suppress the activity of the CbN, it does not follow that increases in Purkinje cell activity would lead to an increase in signal in cerebellar target areas. Although disinhibitory scenarios can be invoked to rationalize such a result, no evidence is provided. Otherwise, strong inhibition at nuclei may evoke postinhibitory rebound and provide time-rocked excitation (Person and Raman, 2011) to subsequent areas, although our data lack *in vivo* electrical activity in multiple regions.

Finally, TNF-α secretion from activated microglia appears to be a potential target for suppressing symptoms associated with high cytokine conditions in the inflamed cerebellum that can cause dysfunctional communication (Figure S6L). It was quite discernible that animals with inflammation in the anterior lobes or in the right hemisphere showed the depression- or autistic-like phenotype, respectively (Figure 7H). Differences in the behavioral abnormality among the regions of acute inflammation should come from projected nuclei after hyperexcitability of the Purkinje neurons. Therefore, our results provide basic information on the effect of inflammation in distinct cerebellar regions and following long-range projections.

STAR★METHODS

Detailed methods are provided in the online version of this paper and include the following:

- KEY RESOURCES TABLE
- LEAD CONTACT AND MATERIALS AVAILABILITY
- EXPERIMENTAL MODEL AND SUBJECT DETAILS
  - Rat
  - Mouse
  - Rat macrophage culture
  - Generation of GO-ATeam2 knock-in mouse
- METHOD DETAILS
  - Patch-clamp recordings
  - Electrophysiological data analysis
  - CSF1R inhibitor treatment
  - Immunohistochemistry
  - Western blotting
  - ATP imaging
  - Drug injection
  - Behavior test battery
- QUANTIFICATION AND STATISTICAL ANALYSIS
- DATA AND CODE AVAILABILITY

SUPPLEMENTAL INFORMATION

Supplemental Information can be found online at https://doi.org/10.1016/j.celrep.2019.07.078.

ACKNOWLEDGMENTS

We thank C. Hansel, M. Mitsuyama, P. Hemant, K. Fujita, T. Inoshita, and T. Hirano for comments on the manuscript and discussions, the Hakubi-center members for discussions, and H. Tanaka for laboratory support. We thank T. Matsui and T. Matsuda for comments and suggestions regarding rs-fMRI analyses and experiments. We thank T. Yamashita for suggestions regarding microglia depletion. We thank M. Taguchi for assistance with experiments and analyses. We thank Biorbyt Ltd. for offering the CSF1R inhibitor for research purposes. fMRI was performed at the Medical Research Support Center, Graduate School of Medicine, Kyoto University, which was supported by the Platform for Drug Discovery, Informatics, and Structural Life Science from the Ministry of Education, Culture, Sports, Science and Technology, Japan. This work was supported by grants from the Kowa Life Science Foundation, the Japanese Society for Promotion of Science (JSPS-KAKENHI, Grant-in-Aid for Young Scientists (A) 26710002), the Brain Science Foundation, the Tokyo Biochemical Research Foundation, the Naito Foundation, and the Hakubi project grant (Kyoto University) (all to G.O.). We received support from PRESTO (JPMJPR14MF to M.Y.), JSPS-KAKENHI (JP17K08786 to M.K.), and the Takeda Science Foundation (to M.K.).

AUTHOR CONTRIBUTIONS

G.O. designed all experiments. G.O. (electrophysiology, immunostaining, western blotting, and animal behavior), M.Y. (ATP imaging and transgenic mice generation), M.K. (western blotting and immunostaining), H.I. (fMRI), and Y.I. (animal behavior) performed the experiments. G.O. (electrophysiology, ATP imaging, immunostaining, animal behavior, and fMRI), M.Y. (ATP imaging), and H.I. (fMRI) analyzed the data. G.O., M.Y., M.K., and H.I. wrote the manuscript.

DECLARATION OF INTERESTS

The authors declare no competing interests.

Received: October 24, 2018
Revised: April 20, 2019
Accepted: July 23, 2019
Published: September 10, 2019

SUPPORTING CITATIONS

The following reference appears in the Supplemental Information: Tikka et al. (2001).

REFERENCES

Aguzzi, A., Barres, B.A., and Bennett, M.L. (2013). Microglia: scapegoat, saboteur, or something else? Science *339*, 156–161.

Arancillo, M., White, J.J., Lin, T., Stay, T.L., and Sillitoe, R.V. (2015). *In vivo* analysis of Purkinje cell firing properties during postnatal mouse development. J. Neurophysiol. *113*, 578–591.

Bagnall, M.W., Zingg, B., Sakatos, A., Moghadam, S.H., Zeilhofer, H.U., and du Lac, S. (2009). Glycinergic projection neurons of the cerebellum. J. Neurosci. *29*, 10104–10110.

Beattie, E.C., Stellwagen, D., Morishita, W., Bresnahan, J.C., Ha, B.K., Von Zastrow, M., Beattie, M.S., and Malenka, R.C. (2002). Control of synaptic strength by glial TNFalpha. Science *295*, 2282–2285.

Beckmann, C.F., and Smith, S.M. (2005). Tensorial extensions of independent component analysis for multisubject FMRI analysis. Neuroimage *25*, 294–311.

Beierlein, M., and Regehr, W.G. (2006). Brief bursts of parallel fiber activity trigger calcium signals in bergmann glia. J. Neurosci. *26*, 6958–6967.

Bellinger, F.P., Madamba, S., and Siggins, G.R. (1993). Interleukin 1 beta inhibits synaptic strength and long-term potentiation in the rat CA1 hippocampus. Brain Res. *628*, 227–234.

Belmeguenai, A., Hosy, E., Bengtsson, F., Pedroarena, C.M., Piochon, C., Teuling, E., He, Q., Ohtsuki, G., De Jeu, M.T., Elgersma, Y., et al. (2010). Intrinsic plasticity complements long-term potentiation in parallel fiber input gain control in cerebellar Purkinje cells. J. Neurosci. *30*, 13630–13643.

Biswal, B., Yetkin, F.Z., Haughton, V.M., and Hyde, J.S. (1995). Functional connectivity in the motor cortex of resting human brain using echo-planar MRI. Magn. Reson. Med. *34*, 537–541.

Boyden, E.S., Katoh, A., and Raymond, J.L. (2004). Cerebellum-dependent learning: the role of multiple plasticity mechanisms. Annu. Rev. Neurosci. *27*, 581–609.

Brown, S.T., and Raman, I.M. (2018). Sensorimotor integration and amplification of reflexive whisking by well-timed spiking in the cerebellar corticonuclear circuit. Neuron *99*, 564–575.e2.

Cao, X., Li, L.P., Wang, Q., Wu, Q., Hu, H.H., Zhang, M., Fang, Y.Y., Zhang, J., Li, S.J., Xiong, W.C., et al. (2013). Astrocyte-derived ATP modulates depressive-like behaviors. Nat. Med. *19*, 773–777.

Chung, W.S., Welsh, C.A., Barres, B.A., and Stevens, B. (2015). Do glia drive synaptic and cognitive impairment in disease? Nat. Neurosci. *18*, 1539–1545.

Daoudal, G., and Debanne, D. (2003). Long-term plasticity of intrinsic excitability: learning rules and mechanisms. Learn. Mem. *10*, 456–465.

De Zeeuw, C.I., and Ten Brinke, M.M. (2015). Motor learning and the cerebellum. Cold Spring Harb. Perspect. Biol. *7*, a021683.

DeNardo, D.G., Brennan, D.J., Rexhepaj, E., Ruffell, B., Shiao, S.L., Madden, S.F., Gallagher, W.M., Wadhwani, N., Keil, S.D., Junaid, S.A., et al. (2011). Leukocyte complexity predicts breast cancer survival and functionally regulates response to chemotherapy. Cancer Discov. *1*, 54–67.

Elmore, M.R., Najafi, A.R., Koike, M.A., Dagher, N.N., Spangenberg, E.E., Rice, R.A., Kitazawa, M., Matusow, B., Nguyen, H., West, B.L., and Green, K.N. (2014). Colony-stimulating factor 1 receptor signaling is necessary for microglia viability, unmasking a microglia progenitor cell in the adult brain. Neuron *82*, 380–397.

Gao, F., Liu, Z., Ren, W., and Jiang, W. (2014). Acute lipopolysaccharide exposure facilitates epileptiform activity via enhanced excitatory synaptic

transmission and neuronal excitability *in vitro*. Neuropsychiatr. Dis. Treat. *10*, 1489–1495.

Grasselli, G., He, Q., Wan, V., Adelman, J.P., Ohtsuki, G., and Hansel, C. (2016). Activity-dependent plasticity of spike pauses in cerebellar Purkinje cells. Cell Rep. *14*, 2546–2553.

Habbas, S., Santello, M., Becker, D., Stubbe, H., Zappia, G., Liaudet, N., Klaus, F.R., Kollias, G., Fontana, A., Pryce, C.R., et al. (2015). Neuroinflammatory TNFα impairs memory via astrocyte signaling. Cell *163*, 1730–1741.

Hansel, C., Linden, D.J., and D'Angelo, E. (2001). Beyond parallel fiber LTD: the diversity of synaptic and non-synaptic plasticity in the cerebellum. Nat. Neurosci. *4*, 467–475.

Hoogland, T.M., Kuhn, B., Göbel, W., Huang, W., Nakai, J., Helmchen, F., Flint, J., and Wang, S.S. (2009). Radially expanding transglial calcium waves in the intact cerebellum. Proc. Natl. Acad. Sci. USA *106*, 3496–3501.

Hoshino, K., Takeuchi, O., Kawai, T., Sanjo, H., Ogawa, T., Takeda, Y., Takeda, K., and Akira, S. (1999). Cutting edge: Toll-like receptor 4 (TLR4)-deficient mice are hyporesponsive to lipopolysaccharide: evidence for TLR4 as the Lps gene product. J. Immunol. *162*, 3749–3752.

Ifuku, M., Hossain, S.M., Noda, M., and Katafuchi, T. (2014). Induction of interleukin-1β by activated microglia is a prerequisite for immunologically induced fatigue. Eur. J. Neurosci. *40*, 3253–3263.

Inoshita, T., and Hirano, T. (2018). Occurrence of long-term depression in the cerebellar flocculus during adaptation of optokinetic response. eLife *7*, e36209.

Ito, M. (2008). Control of mental activities by internal models in the cerebellum. Nat. Rev. Neurosci. *9*, 304–313.

Kato, G., Inada, H., Wake, H., Akiyoshi, R., Miyamoto, A., Eto, K., Ishikawa, T., Moorhouse, A.J., Strassman, A.M., and Nabekura, J. (2016). Microglial contact prevents excess depolarization and rescues neurons from excitotoxicity. eNeuro *3*, 3.

Kelly, R.M., and Strick, P.L. (2003). Cerebellar loops with motor cortex and prefrontal cortex of a nonhuman primate. J. Neurosci. *23*, 8432–8444.

Kettenmann, H., Hanisch, U.K., Noda, M., and Verkhratsky, A. (2011). Physiology of microglia. Physiol. Rev. *91*, 461–553.

Klapal, L., Igelhorst, B.A., and Dietzel-Meyer, I.D. (2016). Changes in neuronal excitability by activated microglia: differential Na(+) current upregulation in pyramid-shaped and bipolar neurons by TNF-α and IL-18. Front. Neurol. *7*, 44.

Koziol, L.F., Budding, D., Andreasen, N., D'Arrigo, S., Bulgheroni, S., Imamizu, H., Ito, M., Manto, M., Marvel, C., Parker, K., et al. (2014). Consensus paper: the cerebellum's role in movement and cognition. Cerebellum *13*, 151–177.

Lalo, U., Palygin, O., Rasooli-Nejad, S., Andrew, J., Haydon, P.G., and Pankratov, Y. (2014). Exocytosis of ATP from astrocytes modulates phasic and tonic inhibition in the neocortex. PLoS Biol. *12*, e1001747.

Ma, L., Gong, H., Zhu, H., Ji, Q., Su, P., Liu, P., Cao, S., Yao, J., Jiang, L., Han, M., et al. (2014). A novel small-molecule tumor necrosis factor α inhibitor attenuates inflammation in a hepatitis mouse model. J. Biol. Chem. *289*, 12457–12466.

Marder, E., Abbott, L.F., Turrigiano, G.G., Liu, Z., and Golowasch, J. (1996). Memory from the dynamics of intrinsic membrane currents. Proc. Natl. Acad. Sci. USA *93*, 13481–13486.

Martina, M., Yao, G.L., and Bean, B.P. (2003). Properties and functional role of voltage-dependent potassium channels in dendrites of rat cerebellar Purkinje neurons. J. Neurosci. *23*, 5698–5707.

Matsui, T., Tamura, K., Koyano, K.W., Takeuchi, D., Adachi, Y., Osada, T., and Miyashita, Y. (2011). Direct comparison of spontaneous functional connectivity and effective connectivity measured by intracortical microstimulation: an fMRI study in macaque monkeys. Cereb. Cortex *21*, 2348–2356.

Monsivais, P., Clark, B.A., Roth, A., and Häusser, M. (2005). Determinants of action potential propagation in cerebellar Purkinje cell axons. J. Neurosci. *25*, 464–472.

Murray, R.Z., Wylie, F.G., Khromykh, T., Hume, D.A., and Stow, J.L. (2005). Syntaxin 6 and Vti1b form a novel SNARE complex, which is up-regulated in activated macrophages to facilitate exocytosis of tumor necrosis Factor-alpha. J. Biol. Chem. *280*, 10478–10483.

Nakano, M., Imamura, H., Nagai, T., and Noji, H. (2011). Ca^{2+} regulation of mitochondrial ATP synthesis visualized at the single cell level. ACS Chem. Biol. *6*, 709–715.

Nakayama, H., Abe, M., Morimoto, C., Iida, T., Okabe, S., Sakimura, K., and Hashimoto, K. (2018). Microglia permit climbing fiber elimination by promoting GABAergic inhibition in the developing cerebellum. Nat. Commun. *9*, 2830.

Neal, M.D., Jia, H., Eyer, B., Good, M., Guerriero, C.J., Sodhi, C.P., Afrazi, A., Prindle, T., Jr., Ma, C., Branca, M., et al. (2013). Discovery and validation of a new class of small molecule Toll-like receptor 4 (TLR4) inhibitors. PLoS ONE *8*, e65779.

Ohno, H., Kubo, K., Murooka, H., Kobayashi, Y., Nishitoba, T., Shibuya, M., Yoneda, T., and Isoe, T. (2006). A c-fms tyrosine kinase inhibitor, Ki20227, suppresses osteoclast differentiation and osteolytic bone destruction in a bone metastasis model. Mol. Cancer Ther. *5*, 2634–2643.

Ohtsuki, G., and Hansel, C. (2018). Synaptic potential and plasticity of an SK2 channel gate regulate spike burst activity in cerebellar Purkinje cells. iScience *1*, 49–54.

Ohtsuki, G., Piochon, C., Adelman, J.P., and Hansel, C. (2012). SK2 channel modulation contributes to compartment-specific dendritic plasticity in cerebellar Purkinje cells. Neuron *75*, 108–120.

Pandey, S., Kawai, T., and Akira, S. (2014). Microbial sensing by Toll-like receptors and intracellular nucleic acid sensors. Cold Spring Harb. Perspect. Biol. *7*, a016246.

Paolicelli, R.C., Bolasco, G., Pagani, F., Maggi, L., Scianni, M., Panzanelli, P., Giustetto, M., Ferreira, T.A., Guiducci, E., Dumas, L., et al. (2011). Synaptic pruning by microglia is necessary for normal brain development. Science *333*, 1456–1458.

Park, B.S., Song, D.H., Kim, H.M., Choi, B.S., Lee, H., and Lee, J.O. (2009). The structural basis of lipopolysaccharide recognition by the TLR4-MD-2 complex. Nature *458*, 1191–1195.

Parkhurst, C.N., Yang, G., Ninan, I., Savas, J.N., Yates, J.R., 3rd, Lafaille, J.J., Hempstead, B.L., Littman, D.R., and Gan, W.B. (2013). Microglia promote learning-dependent synapse formation through brain-derived neurotrophic factor. Cell *155*, 1596–1609.

Pascual, O., Ben Achour, S., Rostaing, P., Triller, A., and Bessis, A. (2012). Microglia activation triggers astrocyte-mediated modulation of excitatory neurotransmission. Proc. Natl. Acad. Sci. USA *109*, E197–E205.

Person, A.L., and Raman, I.M. (2011). Purkinje neuron synchrony elicits time-locked spiking in the cerebellar nuclei. Nature *481*, 502–505.

Piochon, C., Kloth, A.D., Grasselli, G., Titley, H.K., Nakayama, H., Hashimoto, K., Wan, V., Simmons, D.H., Eissa, T., Nakatani, J., et al. (2014). Cerebellar plasticity and motor learning deficits in a copy-number variation mouse model of autism. Nat. Commun. *5*, 5586.

Pribiag, H., and Stellwagen, D. (2013). TNF-α downregulates inhibitory neurotransmission through protein phosphatase 1-dependent trafficking of GABA(A) receptors. J. Neurosci. *33*, 15879–15893.

Prinz, M., and Priller, J. (2017). The role of peripheral immune cells in the CNS in steady state and disease. Nat. Neurosci. *20*, 136–144.

Raman, I.M., and Bean, B.P. (1999). Ionic currents underlying spontaneous action potentials in isolated cerebellar Purkinje neurons. J. Neurosci. *19*, 1663–1674.

Rancz, E.A., and Häusser, M. (2006). Dendritic calcium spikes are tunable triggers of cannabinoid release and short-term synaptic plasticity in cerebellar Purkinje neurons. J. Neurosci. *26*, 5428–5437.

Reis, D.J., Doba, N., and Nathan, M.A. (1973). Predatory attack, grooming, and consummatory behaviors evoked by electrical stimulation of cat cerebellar nuclei. Science *182*, 845–847.

Robertson, P.L., Muraszko, K.M., Holmes, E.J., Sposto, R., Packer, R.J., Gajjar, A., Dias, M.S., and Allen, J.C.; Children's Oncology Group (2006). Incidence and severity of postoperative cerebellar mutism syndrome in children

with medulloblastoma: a prospective study by the Children's Oncology Group. J. Neurosurg. *105* (*6, Suppl*), 444–451.

Saijo, K., and Glass, C.K. (2011). Microglial cell origin and phenotypes in health and disease. Nat. Rev. Immunol. *11*, 775–787.

Santello, M., Bezzi, P., and Volterra, A. (2011). TNFα controls glutamatergic gliotransmission in the hippocampal dentate gyrus. Neuron *69*, 988–1001.

Sarnaik, R., and Raman, I.M. (2018). Control of voluntary and optogenetically perturbed locomotion by spike rate and timing of neurons of the mouse cerebellar nuclei. eLife *7*, e29546.

Schmahmann, J.D. (2004). Disorders of the cerebellum: ataxia, dysmetria of thought, and the cerebellar cognitive affective syndrome. J. Neuropsychiatry Clin. Neurosci. *16*, 367–378.

Schneider, H., Pitossi, F., Balschun, D., Wagner, A., del Rey, A., and Besedovsky, H.O. (1998). A neuromodulatory role of interleukin-1beta in the hippocampus. Proc. Natl. Acad. Sci. USA *95*, 7778–7783.

Schonewille, M., Belmeguenai, A., Koekkoek, S.K., Houtman, S.H., Boele, H.J., van Beugen, B.J., Gao, Z., Badura, A., Ohtsuki, G., Amerika, W.E., et al. (2010). Purkinje cell-specific knockout of the protein phosphatase PP2B impairs potentiation and cerebellar motor learning. Neuron *67*, 618–628.

Silverman, J.L., Yang, M., Lord, C., and Crawley, J.N. (2010). Behavioural phenotyping assays for mouse models of autism. Nat. Rev. Neurosci. *11*, 490–502.

Smith, S.M., and Nichols, T.E. (2009). Threshold-free cluster enhancement: addressing problems of smoothing, threshold dependence and localisation in cluster inference. Neuroimage *44*, 83–98.

Stoodley, C.J., D'Mello, A.M., Ellegood, J., Jakkamsetti, V., Liu, P., Nebel, M.B., Gibson, J.M., Kelly, E., Meng, F., Cano, C.A., et al. (2017). Altered cerebellar connectivity in autism and cerebellar-mediated rescue of autism-related behaviors in mice. Nat. Neurosci. *20*, 1744–1751.

Supple, W.F., Jr., and Kapp, B.S. (1993). The anterior cerebellar vermis: essential involvement in classically conditioned bradycardia in the rabbit. J. Neurosci. *13*, 3705–3711.

Suzuki, L., Coulon, P., Sabel-Goedknegt, E.H., and Ruigrok, T.J. (2012). Organization of cerebral projections to identified cerebellar zones in the posterior cerebellum of the rat. J. Neurosci. *32*, 10854–10869.

Tay, T.L., Mai, D., Dautzenberg, J., Fernández-Klett, F., Lin, G., Sagar, Datta, M., Drougard, A., Stempfl, T., Ardura-Fabregat, A., et al. (2017). A new fate mapping system reveals context-dependent random or clonal expansion of microglia. Nat. Neurosci. *20*, 793–803.

Tikka, T., Fiebich, B.L., Goldsteins, G., Keinanen, R., and Koistinaho, J. (2001). Minocycline, a tetracycline derivative, is neuroprotective against excitotoxicity by inhibiting activation and proliferation of microglia. J. Neurosci. *21*, 2580–2588.

Titley, H.K., Brunel, N., and Hansel, C. (2017). Toward a neurocentric view of learning. Neuron *95*, 19–32.

Tsai, P.T., Hull, C., Chu, Y., Greene-Colozzi, E., Sadowski, A.R., Leech, J.M., Steinberg, J., Crawley, J.N., Regehr, W.G., and Sahin, M. (2012). Autistic-like behaviour and cerebellar dysfunction in Purkinje cell Tsc1 mutant mice. Nature *488*, 647–651.

Tsai, P.T., Rudolph, S., Guo, C., Ellegood, J., Gibson, J.M., Schaeffer, S.M., Mogavero, J., Lerch, J.P., Regehr, W., and Sahin, M. (2018). Sensitive Periods for Cerebellar-Mediated Autistic-like Behaviors. Cell Rep. *25*, 357–367.e4.

Tzour, A., Leibovich, H., Barkai, O., Biala, Y., Lev, S., Yaari, Y., and Binshtok, A.M. (2017). K_V 7/M channels as targets for lipopolysaccharide-induced inflammatory neuronal hyperexcitability. J. Physiol. *595*, 713–738.

Winkler, A.M., Ridgway, G.R., Webster, M.A., Smith, S.M., and Nichols, T.E. (2014). Permutation inference for the general linear model. Neuroimage *92*, 381–397.

Witter, L., and De Zeeuw, C.I. (2015). Regional functionality of the cerebellum. Curr. Opin. Neurobiol. *33*, 150–155.

Womack, M., and Khodakhah, K. (2002). Active contribution of dendrites to the tonic and trimodal patterns of activity in cerebellar Purkinje neurons. J. Neurosci. *22*, 10603–10612.

Womack, M.D., and Khodakhah, K. (2004). Dendritic control of spontaneous bursting in cerebellar Purkinje cells. J. Neurosci. *24*, 3511–3521.

Xanthos, D.N., and Sandkühler, J. (2014). Neurogenic neuroinflammation: inflammatory CNS reactions in response to neuronal activity. Nat. Rev. Neurosci. *15*, 43–53.

Yamamoto, M., Sato, S., Mori, K., Hoshino, K., Takeuchi, O., Takeda, K., and Akira, S. (2002). Cutting edge: a novel Toll/IL-1 receptor domain-containing adapter that preferentially activates the IFN-beta promoter in the Toll-like receptor signaling. J. Immunol. *169*, 6668–6672.

Yirmiya, R., Rimmerman, N., and Reshef, R. (2015). Depression as a microglial disease. Trends Neurosci. *38*, 637–658.

Zerbi, V., Grandjean, J., Rudin, M., and Wenderoth, N. (2015). Mapping the mouse brain with rs-fMRI: An optimized pipeline for functional network identification. Neuroimage *123*, 11–21.

Zhan, Y., Paolicelli, R.C., Sforazzini, F., Weinhard, L., Bolasco, G., Pagani, F., Vyssotski, A.L., Bifone, A., Gozzi, A., Ragozzino, D., and Gross, C.T. (2014). Deficient neuron-microglia signaling results in impaired functional brain connectivity and social behavior. Nat. Neurosci. *17*, 400–406.

Zhang, Z., Chen, G., Zhou, W., Song, A., Xu, T., Luo, Q., Wang, W., Gu, X.S., and Duan, S. (2007). Regulated ATP release from astrocytes through lysosome exocytosis. Nat. Cell Biol. *9*, 945–953.

Zhang, J., Malik, A., Choi, H.B., Ko, R.W., Dissing-Olesen, L., and MacVicar, B.A. (2014). Microglial CR3 activation triggers long-term synaptic depression in the hippocampus via NADPH oxidase. Neuron *82*, 195–207.

Zheng, N., and Raman, I.M. (2010). Synaptic inhibition, excitation, and plasticity in neurons of the cerebellar nuclei. Cerebellum *9*, 56–66.

STAR★METHODS

KEY RESOURCES TABLE

REAGENT or RESOURCE	SOURCE	IDENTIFIER
Antibodies		
Rabbit anti-Iba1:red fluorescent probe 635	Wako	Cat# 013-26471, RRID:AB_2687911
Rabbit anti-Calbindin:Alexa Fluor® 488	Abcam	Cat# ab208377, RRID:AB_2750567
Rabbit polyclonal, anti-rat TNF-α	eBioscience	Cat# BMS175, RRID:AB_10596988
Goat polyclonal, anti-rat IL-6	R&D	Cat# AF506, RRID: AB_355398
Goat polyclonal, anti-rat IL-1β	R&D	Cat# AF-501-NA, RRID: AB_354508
Chemicals, Peptides, and Recombinant Proteins		
Anisomycin	Tocris	Cat# 1290, CAS: 22862-76-6
Apamin	Tocris	Cat# 1652, CAS: 24345-16-2
Apocynin	Tocris	Cat# 4663, CAS: 498-02-2
Cycloheximide	Tocris	Cat# 0970, CAS: 66-81-9
Cyclosporin A	Tocris	Cat# 1101, CAS: 59865-13-3
C34	Tocris	Cat# 5373, CAS: 40592-88-9
C87	Tocris	Cat# 5484, CAS: 332420-90-3
Minocycline hydroxide	Tocris	Cat# 3268, CAS: 13614-98-7
MRS 2179 tetrasodium salt	Tocris	Cat# 0900, CAS: 1454889-37-2
NBQX disodium salt	Tocris	Cat# 1044, CAS: 479347-86-9
Picrotoxin	Tocris	Cat# 1128, CAS: 124-87-8
PPADS tetrasodium salt	Tocris	Cat# 0625, CAS: 192575-19-2
Tetrodotoxin citrate	Tocris	Cat# 1069, CAS: 18660-81-6
Okadaic acid	AdipoGen	Cat# AG-CN2-0060, CAS: 78111-17-8
ATP (Adenosine 5′-triphosphate disodium salt)	Sigma-Aldrich	Cat# 10127523001, CAS: 51963-61-2
BAPTA	Sigma-Aldrich	Cat# A4926, CAS: 85233-19-8
L-2-Aminoadipic acid	Sigma-Aldrich	Cat# A7275, CAS: 1118-90-7
Ki20227	Biorbyt	Cat# orb181032, CAS: 623142-96-1
LPS from *E. coli O26*	Wako	Cat# 120-05131
LPS from *E. coli O111*	Wako	Cat# 125-05201
Recombinant rat TNF-α protein, carrier-free	R&D Systems	Cat# 510-RT/CF
Heat-killed *E.coli 0111:B4* (HKEB)	InvivoGen	Cat# tlrl-hkeb2
Heat Killed *Pseudomonas aeruginosa* (HKPA)	InvivoGen	Cat# tlrl-hkpa
Heat Killed *Streptococcus pneumoniae* (HKSP)	InvivoGen	Cat# tlrl-hksp
Peptidoglycan from *E. coli 0111:B4* (PGN-EB)	InvivoGen	Cat# tlrl-pgneb
CF®555 Dye-Dextran 10,000 MW	Biotium	Cat# 80112
Experimental Models: Cell Lines		
NR8383 [AgC11x3A, NR8383.1]	ATCC	Cat# CRL-2192, RRID: CVCL_4396
Experimental Models: Organisms/Strains		
Rat: Sprague-Dawley	Japan SLC	Slc:SD
Mouse: C57BL/6J	Japan SLC	C57BL/6JJmsSlc
Mouse: TLR2 knockout mice	Oriental Bio Service	RRID: IMSR_OBS:3
Mouse: TLR4 knockout mice	Oriental Bio Service	RRID: IMSR_OBS:4
Mouse: MyD88 knockout mice	Oriental Bio Service	RRID: IMSR_OBS:1
Mouse: TRIF knockout mice	Oriental Bio Service	RRID: IMSR_OBS:16
Mouse: GO-ATeam2 knockin mice	This paper	N/A

(*Continued on next page*)

Continued

REAGENT or RESOURCE	SOURCE	IDENTIFIER
Software and Algorithms		
MATLAB	Mathworks	RRID:SCR_001622
SPM12	the Wellcome Centre for Human Neuroimaging	RRID:SCR_007037
FSL	the Analysis Group, FMRIB, Oxford, UK.	RRID:SCR_002823
MELODIC toolbox in the FSL platform		https://fsl.fmrib.ox.ac.uk/fsl/fslwiki/MELODIC
Multi Gauge ver.3.2	Fujifilm	RRID:SCR_014299

LEAD CONTACT AND MATERIALS AVAILABILITY

Further information and requests for resources and reagents should be directed to and will be fulfilled by the Lead Contact, Gen Ohtsuki (gohtsuki@neurosci.biophys.kyoto-u.ac.jp or ohtsuki.gen.7w@kyoto-u.ac.jp).

EXPERIMENTAL MODEL AND SUBJECT DETAILS

Rat

Male Sprague-Dawley rats were used for the experiments. Postnatal (P)22–28 days old rats were used for patch-clamp recordings and western blotting. Microglia depletion experiment started at P19–20 days. Behavior battery tests and MR imaging were conducted at P22–26 days.

Mouse

Male C57BL/6J, GO-ATeam2 (*Related study is in preparation for submission*), TLR2$^{-/-}$, TLR4$^{-/-}$, MyD88$^{-/-}$ (Hoshino et al., 1999), and TRIF$^{-/-}$ (Yamamoto et al., 2002) mice (Oriental Bioservice, Inc., Japan) were used for the experiments. P2-month-old mice were used for patch-clamp recordings, ATP-imaging and immunohistochemistry. Microglia depletion experiment were started at P5- to P6-week.

Animals were housed (5 animals at maximum in each cage) and maintained under a 12-h light: 12-h dark cycle, at a constant temperature and humidity (20–24°C, 35%–55%), with food and water available *ad libitum*. All procedures were performed in accordance with the guidelines of the Animal Care and Use Committees of the Kyoto University and were approved by the Ethical Committee of the Kyoto University. All animal handling and reporting comply with ARRIVE guidelines.

Rat macrophage culture

NR8383 [AgC11x3A, NR8383.1] (ATCC) was used for the control of the cytokine release (western blotting) in response to LPS administration (*data not shown*). F-12K medium was used for the culture medium.

Generation of GO-ATeam2 knock-in mouse

An ATP probe (GO-ATeam2) was developed for use in conjunction with green and orange fluorescent proteins as a fluorescence/Förster resonance energy transfer (FRET) pair (Nakano et al., 2011). We newly generated GO-ATeam2 transgenic mice to monitor the ATP concentration in living animals. Briefly, we employed a knock-in strategy targeting the Rosa26 locus and the CAG promoter to regulate transcription. We used the GeneArt Seamless Recombination System (Thermo Fisher Scientific) to create GO-ATeam2 knock-in mice. The targeting vector was induced into G4 ES cells with electroporation. The constructs harbored by the ES clones underwent homologous recombination, which was confirmed by Southern blot analysis using appropriate probes (provided by K. Hoshino and T. Kaisho, Osaka University), PCR, and qPCR. Male chimeras derived from each ES cell line were bred with C57BL/6J females, yielding heterozygous F1 offspring (C57BL/6J × 129 background).

METHOD DETAILS

Patch-clamp recordings

In vitro patch-clamp recordings were obtained as described previously (Belmeguenai et al., 2010; Ohtsuki et al., 2012). Sagittal slices of the cerebellar vermis (250 μm) were prepared from Sprague-Dawley rats (postnatal (P)22–28 days old) after isoflurane anesthesia and decapitation (Figures 1, 3A–3G, 3N–3S, 4A–4F, 4J–4O, 5, S1, S2G, S2H, S5C, S5D, and S5F). In some experiments, C57BL/6J, TLR2$^{-/-}$, TLR4$^{-/-}$, MyD88$^{-/-}$, and TRIF$^{-/-}$ mice (P2-month-old) were used (Figures 2C–2E, 4G–4I, 5C–5G, and S4A–S4D). Slices were cut on a vibratome (Dosaka EM, Japan) using ceramic blades. Subsequently, slices were kept in artificial cerebrospinal fluid

(ACSF) containing the following (in mM): 124 NaCl, 5 KCl, 1.25 Na_2HPO_4, 2 $MgSO_4$, 2 $CaCl_2$, 26 $NaHCO_3$, and 10 $_D$-glucose, bubbled with 95% O_2 and 5% CO_2. During cutting, supplemental ingredients (5 mM Na-ascorbate, 2 mM thiourea, and 3 mM Na-pyruvate) were added to the ACSF. After at least 1-h, slices were transferred to a recording chamber superfused with ACSF at near-physiological temperature (32–34°C). The ACSF was supplemented with 100 μM picrotoxin to block $GABA_A$ receptors. Patch-clamp recordings were performed under a × 40 water immersion objective lens equipped with a DIC system (DS-Qi2; Nikon) mounted on a microscope (ECLIPSE FN1, Nikon). Recordings were performed in voltage-clamp or current-clamp mode using an EPC-10 amplifier (HEKA Elektronik, Germany). Membrane voltage and current were filtered at 2.9 kHz, digitized at 10 kHz, and acquired using Patchmaster software (HEKA Elektronik). Patch pipettes (borosilicate glass) were filled with a solution containing (in mM): 9 KCl, 10 KOH, 120 K-gluconate, 3.48 $MgCl_2$, 10 HEPES, 4 NaCl, 4 Na_2ATP, 0.4 Na_3GTP, and 17.5 sucrose (pH 7.25 titrated with 1 M KOH). Membrane voltage was offset for liquid junction potentials (11.7 mV). Somatic patch electrodes had electrode resistances of 2–4 MΩ, while dendritic patch electrodes had electrode resistances of 7–8 MΩ (Ohtsuki et al., 2012). Hyperpolarizing bias currents (100–400 pA) were injected to stabilize the somatic membrane potential at approximately −75 to −80 mV and to prevent spontaneous spike activity. To obtain the firing frequency in response to different levels of depolarization (Figures 1B, 1E, 2C, 3A, 3P, S4A–S4D, S5C, S5D, and S5F), we applied 500-ms pulses ranging from 0 to 550 pA every 2 or 3 s, which were increased by 50 pA per step, and counted the number of simple spike-shaped action potentials. Action potential on dendrites were recorded by simultaneous patch-clamping from soma and dendrite (Figures 1H and 1I). Data were collected at distances of 80–120 μm apart from the soma at secondary and tertiary branches. Due to the lack of voltage-sensitive Na^+ channels, the amplitude of bAPs attenuates in a distance-dependent manner. Approximate curves were obtained from entire recordings including somatic APs, by fitting to the single exponential function, are superimposed to the plotting of control (black line), apamin (orange line) and LPS (magenta line) experiments in Figure 1I. To examine the excitability of Purkinje cells from drug-injected cerebella, slices were prepared within 1 h following injection, and recordings were obtained for 1–5 h. In the other *ex vivo* experiments, we tested the excitability at 24–32 hours after injection. Rheobase from the basal potential and the slope of the gain function against depolarization pulses from 50 to 250 pA were also measured (Tables S1 and S2). For long-term recording (Figures 1C, 1D, 1F, 1G, 2D, 2E, 3B–3G, 3N, 3Q–3S, 5A–5G, S1, S2G, and S2H), depolarizing current steps (100–400 pA/500 ms) were applied every 20 s to the soma to evoke action potentials. In some experiments, for the conditioning of intrinsic plasticity induction, depolarizing pulses (300–550 pA/100 ms) were applied at 5 Hz for 4 s. We compared firing frequency normalized by 5-min average before 0 min (i.e., −5 – −1 min) to that of 25 to 30 min later. Input resistance was monitored by administering 50-pA hyperpolarizing pulses (50-ms duration) following the depolarization (Figures 5K and 5L). Data were discarded when the input resistance had changed more than 20%. Membrane potential was kept at approximately −75 to −80 mV within 5% changes throughout each experiment (Figures 5M and 5N). All drugs were applied to the bath chamber via the circulation system. Heat-killed bacteria (HKEB, *E.coli 0111:B4*; HKPA, *P. aeruginosa*; HKSP, *S. pneumoniae*) and peptidoglycan (PGN, peptidoglycan from *E. coli 0111:B4*) were purchased from InvivoGen, and 10^{10} freeze-dried cells were diluted to 10^7 cells/mL in sterile, endotoxin-free water, for *in vitro* application. Heat-killed Gram-negative bacteria mixture (HKGn; HKEB + HKPA) was applied *in vitro* at the concentration of 10^7 cells/mL for each. For the recording of spontaneous EPSC (sEPSC) and miniature EPSC (mEPSC) events (Figure 4), membrane current was held at −71.7 mV or at −81.7 mV only if the membrane current was jittered, and current was recorded for 1.5 s trials, for at least 180 s in total. mEPSC was monitored under suppression of the neuronal activity by TTX citrate (0.5 μM).

Electrophysiological data analysis

Data were analyzed using a custom program written in MATLAB (Mathworks). For the analysis of action-potential waveforms, we measured the first action potential evoked by administration of a 200–400-pA depolarizing pulses. Action potential analysis was performed as described previously (Belmeguenai et al., 2010) (Tables S1 and S2). For the analysis of sEPSC and mEPSC events, periods of fluctuation were omitted and supplemented by other trials. Then, a Savitzky-Golay filter (*sgolayfilt*) was applied to the recorded currents. The event detection threshold for s/mEPSCs was set at 4.5 pA. Events were defined as those exceeding four standard deviations during the 10 ms pre-period. We then applied the *fminsearch* function to obtain decay time by a single exponential. If the current trace at the decay period (limited to 19 ms) was poorly fit, the data were excluded. Detected cell numbers and event numbers of sEPSC are 35 (46058), 13 (30718), 12 (30229), 15 (39107), 16 (36699), 13 (30588), 16 (22960), 14 (25040), 15 (36889), 18 (25826) in control, LPS, PGN, TNF-α, HKEB, HKPA, HKSP, minocycline+LPS, ATP, and PPADS+LPS conditions, respectively. Event numbers are in the parentheses. Those of mEPSC are 13 (4123), 16 (32017), 13 (29652), 16 (34876), 13 (24808), 12 (10240), 14 (10321), 14 (36756), 13 (16773) in control, LPS, TNF-α, HKEB, HKPA, HKSP, minocycline+LPS, ATP, and PPADS+LPS conditions, respectively. Rise time was regarded as the period spanning 10%–90% of the change from peak to basement values. Rise time, half-width, and decay time of s/mEPSCs were not significantly different against control except for ATP (*data not shown*). Representative sEPSC/mEPSC traces in Figures 4B and 4K are the average from 1571/255, 946/454, 1264, 1330/904, 1132/477, 1079/393, 663/358, 276/611, 1634/296, and 619/438 events of control, LPS, PGN, TNF-α, HKEB, HKPA, HKSP, minocycline+LPS, ATP, and PPADS+LPS conditions, respectively. For the cumulative probability in Figures 4D, 4F, 4M, and 4O, a maximum of 400 sEPSC and 800 mEPSC amplitude and frequency events were collected from each cell for each experiment.

CSF1R inhibitor treatment

For the sake of pharmacological microglia-depletion, the CSF1R inhibitor Ki20227 (Ohno et al., 2006; Elmore et al., 2014) (Biorbyt Ltd., UK) was given to P5- to P6-week C57BL/6 mice via the drinking water (100 or 250 mg/L, including 2.5% sucrose) or by oral

administration 0.2 mL/day (20 mg/mL dissolved to 10% DMSO and 90% corn oil) for 6–7 days (Figures 2A, 2B, and S2A–S2F). Ki20227 (IC_{50} = 2 nM to M-CSF receptor; 451 nM to c-Kit) (Ohno et al., 2006) is a more potent and specific inhibitor to CSF1R than PLX3397 (IC_{50} = 20 nM to M-CSF receptor; 10 nM to c-Kit) (DeNardo et al., 2011). A few mice were given the inhibitor for 11–12 days for electrophysiological experiments. In some experiments, we gave Ki20227 0.2 mL/day (oral administration of 20 mg/mL with 10% DMSO and 90% corn oil) to male juvenile Sprague-Dawley rats (38-62 g body weight) from P19–20 for 5 days. Following reagent administration under specific pathogen free (SPF)-environment, we sacrificed animals for electrophysiological and immunohistochemical experiments, and we conducted behavior tests with rats. No obvious behavioral or health problems were observed during the Ki20227 treatment, except for a reduction of weight in a few rats with vulnerability whose data were excluded.

Immunohistochemistry

Immunostaining was performed as described (Belmeguenai et al., 2010), with some modifications. After perfusion fixation of the control and Ki20227-treated mice with 4% paraformaldehyde (PFA), brains were kept in PFA for 2 days at 4°C. After submersion in phosphate buffered saline (PBS) containing 30% sucrose for 2–4 days, 50-μm cryosections were collected in water. Sections were heated in HistoVT (Nacalai Tesque, Japan) to 80°C for 30 min, rinsed in TBS, and incubated in blocking solution (TBS containing 10% normal goat serum (NGS) and 0.5% Triton) for 1 h at 20–24°C. Sections were then incubated with fluorescently conjugated-primary antibodies against Iba1 (rabbit anti-Iba1:red fluorescent probe 635, 1:200 [2.5 μg/mL]; Wako) and Calbindin (rabbit anti-Calbindin:Alexa Fluor® 488, 1:100 [5 μg/mL]; Abcam) at 4°C for 48 h. Subsequently, sections were rinsed three times in PBS for 5 min each and were mounted on glass slides and coverslipped. Fluorescence images were obtained using a Zeiss LSM 780, Olympus FV1000 or Olympus FV 3000 confocal laser-scanning microscope equipped with Plan-Apochromat 20 × /0.8 and 10 × /0.4 lenses. Emission wavelength for imaging was 488 and 639 nm, and the fluorescence was filtered using 640-nm low-pass and 490–555-nm band-pass filters. Individual images were taken under a fluorescence microscope (FV 3000), and the merged-images are shown as whole cerebellar images in Figure S2. For counting the number of microglia in Figure 2B, arbitral parts of the cerebellum were imaged (489.5 × 489.5 μm) with z stacks of 24–30 images at every 1 μm, and the density of microglia were calculated from 43–54 regions of interest (ROIs) (from 2 mice per group), excluding white matter.

Western blotting

Cerebellar slices from Sprague-Dawley rats (P24–25 days old) were prepared as described above. After recovery, brain slices were incubated in normal ACSF or LPS-containing ACSF for 0, 20, or 60 min at near-physiological temperature. Supernatants were concentrated with Amicon Ultra-15 Centrifugal Filter Units (EMD Millipore) and subjected to immunoblotting analysis using anti-rat TNF-α (BMS175; eBioscience), anti-rat IL-6 (AF506; R&D) and anti-rat IL-1β (AF-501-NA; R&D). Intensity was quantified using Multi Gauge ver.3.2 (Fujifilm). For a control experiment, we used rat macrophage culture (NR8383 [AgC11x3A, NR8383.1], ATCC) (*data not shown*).

ATP imaging

For FRET imaging with the ATP probe in the cerebellum, P2–3 weeks GO-ATeam2 mice were decapitated after inhalation of 2% isoflurane, following which whole brains were isolated. The cerebellum was placed in cooled ACSF solution as described for the electrophysiological experiments. Air stones (#180; Ibuki) were used for aeration (95% O_2 and 5% CO_2). Sagittal slices were cut to a thickness of 300 μm using a vibratome (VT 1000S; Leica), following which they were maintained for at least 30 min at room temperature in ACSF solution. FRET imaging was performed on a two-photon microscope (TCS SP8; Leica). The imaging chamber was set on the stage of the microscope with flowing ACSF solution bubbled with 95% O_2 and 5% CO_2. LPS (final concentration 12 μg/mL) or a mixture of HKEB and HKPA (final 10^7 cells/mL, for each) were added to the ACSF. Exciting light (920 nm, 25 W under objective lens) was applied, and the molecular layer (ML) and granule cell layer (GL) of the cerebellum were scanned every 2 min. Images were obtained from individual locations (scanned area size, 550 × 550 μm). We used BP525/50 filters for emission, and DM560 and D585/40 filters for excitation fluorescence separation. IMD images and quantifying images were developed from the fluorescence images using MetaMorph software (Roper Scientific, Trenton, NJ). FRET signals at the chosen ROI (whose shape depended on the target area, Figure S3H) in the ML and GL were averaged, and the obtained ratio was applied to the following equation: FRET ratio = 1.52 × [ATP]^1.7 / ([ATP]^1.7 + 2.22) + 0.44, and then, ATP concentration was calculated. The coefficients were carefully determined based on two methods. First, mouse embryonic fibroblasts were obtained from GO-ATeam2 mice. After piercing the fibroblast membrane, we applied different concentrations of ATP, monitored the FRET ratio, and determined coefficients based on the function for fitting ATP concentration to the FRET ratio. Second, we performed a luciferase assay of ATP concentration (Tissue ATP assay kit; TOYO B-NET) in fertilized eggs from GO-ATeam2 mice. Mice were injected with ATP synthetase inhibitors (2DG plus antimycin A), and the time course of the FRET ratio was monitored. Coefficients obtained by the two methods were substantially identical, indicating that they were appropriate for use in the present study. Our ATP imaging with transgenic mice expressing ATP probes monitored the ATP concentration in the cytosol, insomuch as no specific promoters were tied to the transgene construct. Control fluorescence images were obtained prior to drug exposure (n = 9 in ML, and n = 10 in GL) and used for subtraction of the background signal. Following endotoxin exposure, remnants on the tubing and chamber were cleaned with 80% ethanol for at least 5 min. To visualize the time courses of ΔATP, baseline ATP was set to zero (−6 to −2 min).

Drug injection

Rats received an injection of 0.20–0.30 μL of PBS, LPS (1 mg/mL), a mixture of heat-killed Gram-negative bacteria (HKEB and HKPA, 10^9 cells/mL for each), a TNF-α inhibitor (C87, 2–4 mM), TNF-α (20 μg/mL) and ATP (20 mM) into the vermis or right hemisphere of the cerebellum. Drugs were injected under anesthesia with 0.9% ketamine (Daiichi Sankyo Co., Ltd.) and 0.2% xylazine (Bayer AG) (*i.p.*, 5.3 ± 0.5 μL/g of body weight, as mean ± std.). We started surgery after animals' breath and pulse were stabilized and the extent of anesthesia was enough, without corneal reflection, touch, and pinch responses. For vermal injection into cerebella, rats were fixed to the stereotaxic apparatus and a small hole (300 μm radius) was drilled in the skull (2.5 mm posterior to lambda), following which a microsyringe was inserted forward to the anterior lobule (3.0–3.3 mm depth at 86°, lobule II–IV) or to the posterior lobule (6.3–6.5 mm depth at 65°, lobule VIII–IX) (Ifuku et al., 2014). To clarify the localized spread of the reagent, we did the post-injection histology, and we confirmed the dextran-conjugated CF®555 dye (0.30ul, 0.5%; Biotium, CF®555 Dextran 10,000 MW) was restricted in the targeted anterior lobes through the depth of 3.4 mm to 0.4 mm from the pial surface, in two animals. Representative vermal section is shown in Figure S5G. For injection into the right and left hemispheres, a hole was made at 3.0–3.5 mm posterior to the lambda and around 1.5 mm lateral, putting forward to 4.0 mm with an angle of 60–65°. The wound was sealed with Spongel (Astellas Pharma Inc.), after which the animal was allowed to rest in a clean cage. A heat-plate was used to maintain body temperature, if necessary. Rats woke up approximately 40 min after injection of the ketamine/xylazine. We handled animals very carefully and treated them with as little discomfort as possible. After at least 2 h of recovery, we confirmed that the effects of the anesthesia had dissipated and that no paralysis or seizures had occurred, following which the behavior test battery (open field test, social interaction test, forced swim test, marble burying test, retention test on balance beam, and gait analysis) was initiated. Forced swim test was conducted last in the battery, to avoid the effect of fear conditioning itself. Gait analysis and retention test on balance bar after recovery revealed no obvious ataxia and motor discoordination (Figures 7E, S5A, S5B, S6F, and S6K).

Behavior test battery

Open field test

We monitored the spatial exploratory behavior of Sprague-Dawley rats (P22–26 days) weighing 52–86 g and microglia-depleted rats (P24–25 days). After habituation in the experimental room (1 h), rats were individually placed on the center of the Plexiglas open field arena (72 × 72 cm^2, 30 cm high white walls with black floor), following the operation. We monitored the behavior of freely moving rats for 30 min using a video camera. The distance traveled, resting period, moving period, and mean speed were compared among the groups. The arena and surrounding walls were cleaned and deodorized with H_2O and 70% EtOH before each session. Exploration behavior was quantified using Smart 3.0 software (Panlab Harvard Apparatus). The resting state was defined at that during which moving speed fell below the threshold of 2.5 cm/s. A total of 13, 11, 11, 11, 12, 15, 12, 16, 14, 12,15 and 13 animals was included in the non-conditioned (NC), PBS, LPS, heat-killed Gram-negative bacteria mixture (HKGn; HKEB+HKPA), HKGn+C87, TNF-α, ATP, microglia-depleted (dMG)+LPS, LPS to hemisphere, LPS to posterior lobes, dMG and C87 conditions, respectively. A total of 15, 14, 17 and 10 animals was included in the PBS, LPS, heat-killed Gram-negative bacteria mixture (HKGn) and HKGn+C87 conditions on the following day, respectively (Figure S5E).

Social interaction

The sociability of rats was tested in a Plexiglas open-field arena (72 × 72 cm^2, 30 cm high) with small circular wire cages (15 cm in diameter, 20 cm high) in two corners. First, animals were allowed to explore the arena for 3 min to determine the baseline of exploratory behavior against the novel subjects without social targets. All movements were recorded with video-tracking. We defined a preferred corner area as one area (30 × 36 cm^2 square around a wire cage) where the animal spent more time during the baseline period. Next, a sibling rat was placed into one cage that was less preferred during the baseline period, and movements were monitored for another three minutes. In this social approach model, time spent in the interaction and overall locomotion were compared by an examiner in a blinded experimental condition. Sociability index was calculated by dividing the time difference between time spent in the interaction zone and in other areas with and without a sibling by total time, as following;

$$\text{Sociability index} = \left(\left(Ta^{test} - \overline{Ta}^{test}\right) - \left(Ta^{baseline} - \overline{Ta}^{baseline}\right)\right) / T^{total},$$

where T as the resident time (sec), Ta^{test} as time spent in the area where the sibling caged in the test period, $\overline{Ta}^{test}$ as time spent out of the area where the sibling is caged, and T^{total} as 180 s. $Ta^{baseline}$ and $\overline{Ta}^{baseline}$ are those in the baseline period. In Figure 6C, abbreviations are given in the equation of sociability index. A total of 15, 15, 12, 13, 16, 13, 16, 14, 14, 17 and 13 animals was included in the PBS, LPS, HKGn, HKGn+C87, TNF-α, ATP, dMG+LPS, LPS to hemisphere, LPS to posterior lobes, dMG and C87 conditions, respectively.

Same corner preference

We tested the preference of the place where animals continue to locate in the platform of the social interaction test. First, we defined a preferred corner area (5 × 5 cm^2 square: SW, SE, NW and NE) as a corner where the animal spent more than 1 min during the baseline period. In the next session, with a sibling rat in one wire cage, we measured the time when rats spent in the same corner where they preferred, and we scored the time in second as the index. When one has no preferred corner in the first session, the sore is zero. A total of 15, 15, 12, 13, 16, 13, 16, 14, 14, 17, and 13 animals was included in the PBS, LPS, HKGn, HKGn+C87, TNF-α, ATP, dMG+LPS, LPS to hemisphere, LPS to posterior lobes, dMG and C87 conditions, respectively.

Sniffing

We measured the time in second when rats spent around the wire cage with a sibling animal in the second session of the social interaction test. We included the time when rats interacted to and sniffed the sibling, and we excluded the time during grooming or scratching. A total of 15, 14, 11, 13, 16, 13, 16, 14, 14, 17, and 13 animals was included in the PBS, LPS, HKGn, HKGn+C87, TNF-α, ATP, dMG+LPS, LPS to hemisphere, LPS to posterior lobes, dMG and C87 conditions, respectively.

Forced swim

FS test were conducted in a 5 L plastic beaker filled with 4.3 L of water (16.5 cm in diameter, 20-cm-depth, 24.1 ± 0.2°C). Rats were tested swimming for 8 min and video-recorded. Total duration of immobility, each of which is more than 1 s, in the last 4 min was measured in a blinded condition. A total of 15, 15, 16, 14, 16, 13, 16, 10, 13, 17, and 13 animals was included in the PBS, LPS, HKGn, HKGn+C87, TNF-α, ATP, dMG+LPS, LPS to hemisphere, LPS to posterior lobes, dMG and C87 conditions, respectively.

Marble burying

Marble burying (MB) is a test for stereotyped repetitive behaviors in rodents analogous to those observed in autistic phenotypes (Silverman et al., 2010). MB tests were conducted in a testing cage (26 × 18.2 cm^2, 13-cm-high). Bedding tips as wood shavings were covered to a depth of 3 cm. 20 glass marbles (17 mm in diameter) were aligned equidistantly in four rows of five marbles each. Spaces (4–5 cm width) were made for placing animals. At the end of the 20-min test period, rats were carefully removed from the cages. The marble burying score was defined as the following: 1 for marbles covered > 50% with bedding, 0.5 for marbles covered ~50% with bedding, and 0 for marbles less covered. A total of 24, 16, 15, 16, 13, 15, 13, 14, 19, 13, 17 and 13 animals was included in the NC, PBS, LPS, HKGn, HKGn+C87, TNF-α, ATP, dMG+LPS, LPS to hemisphere, LPS to posterior lobes, dMG and C87 conditions, respectively.

Retention test on balance beam

Time in seconds was measured while rats remained on a wooden balance beam with 25 mm diameter placed at a height of ~11 cm. Measurement time is 5 minutes after animals became calm on the beam. Trials in which animals escaped were not analyzed. A total of 12, 10, 12, 10, 16, 11, 13, 13, 12, 13 and 13 animals was included in the PBS, LPS, HKGn, HKGn+C87, TNF-α, ATP, dMG+LPS, LPS to hemisphere, LPS to posterior lobes, dMG and C87 conditions, respectively (Figures 7E, S5A, S5B, S6F, and S6K).

Gait analysis

Animals were placed at the end of one directional passageway (8.5 cm in width and 30 cm in length) with a transparent floor at a height of 13 cm, and they were allowed to walk straight forward while being recorded with a micro video camera from below. Each animal was tested three times for walking. Centers of paw positions (forepaws and hind paws) were measured, and three or four strides lengths for each trial were collected and averaged from 6, 6, 6, 7, 7, and 7 rats of PBS, LPS, HKGn, HKGn+C87, dMG+LPS, and LPS to hemispheres conditions (Figures S5B).

MR imaging and data analyses

We used anaesthetized Sprague-Dawley rats as described in the open field test, with three experimental groups of non-conditioned (NC, n = 13 animals), HKGn-injected (HKGn, n = 12 animals), and HKGn+C87-injected (HKGn+C87, n = 14 animals) rats. After a 2-h recovery period from the ketamine and xylazine anesthesia as described above, rats inhaled isoflurane (2% for induction: 1% for MR imaging (MRI)) in a mixture of 66% air and 34% oxygen at 1.5 L/min with ventilation, were stabilized by head-holding in a plastic tube, and were monitored for respiratory rate (52–109 breaths/min) and body temperature (30–34°C). Rats were scanned with a 7.0 T MRI scanner (Bruker BioSpin) with a quadrature transmit-receive volume coil (35 mm inner diameter). To make the main magnetic field more homogeneous, shimming was performed in a 20 × 15 × 10 mm^3 region by mean of a local MapShim protocol using a previously acquired field map. Resting-state *f*MRI is useful to study the functional network in the brain. This network has been shown to be spontaneously activated without stimulation. Spontaneous low frequency fluctuations (< 0.1 Hz) in the blood-oxygen-level dependent (BOLD) signals of some regions are known to synchronize with each other. Such correlation of the BOLD signals is considered as a manifestation of functional connectivity of the brain (Biswal et al., 1995). BOLD rs-*f*MRI time series were obtained with a single-shot gradient-echo planar imaging (EPI) sequence (repetition time [TR]/echo time [TE] = 1.0 s/9 ms; flip angle, 60°; matrix size, 80 × 64; field of view [FOV], 2.5 × 2.0 cm^2; 12 coronal slices from top to bottom; slice thickness, 1 mm; slice gap 0 mm) for 6–8 min with a total 360–480 volumes. Following the EPI sequence twice, high-resolution anatomical images for each experimental animal were obtained using a 2D multi-slice T_2-weighted (T2W) fast-spin echo sequence (RARE) (TR/TE = 3.0 s/36 ms; matrix size, 240 × 192; FOV, 2.5 × 2.0 cm^2; 24 coronal slices; slice thickness, 0.50 mm; slice gap 0 mm; with fat suppression by frequency selective pre-saturation) under 2.0% isoflurane inhalation. To image the region of inflammation, we used a fluid attenuation inversion recovery (FLAIR) sequence, which suppresses cerebrospinal fluid effects on the image (inversion time [TI] = 2.5 s; TR/TE = 10 s/36 ms; matrix size, 240 × 192; FOV, 2.5 × 2.0 cm^2; 24 coronal slices; slice thickness, 0.50 mm; slice gap 0 mm; with fat suppression by frequency selective pre-saturation). FLAIR is an MRI sequence in which the signals of cerebrospinal fluid is virtually zeroed by elongating the inversion time, TI. With the combination of this sequence and fat suppression, it is more useful to discern infarction, hemorrhages, encephalitis, cerebellitis, and meningitis from the images than the T_2-weighted sequences, in clinical applications and even in the animal disease models. In general, an infection of the bacteria and the resultant destruction of tissues would increase the vascular permeability beneath the lesion. The released exudate produces a localized edema (inflammatory edema), which includes the abundant liquid, generating high T_2-signal. In FLAIR images, the high signal intensity is depicted by white.

Image data from three experiments of NC, HKGn-injected and HKGn+C87-injected were analyzed with SPM12 (http://www.fil.ion.ucl.ac.uk/spm), FSL (https://fsl.fmrib.ox.ac.uk/fsl/fslwiki/FSL), and in-house software written with MATLAB (MathWorks).

We pre-processed imaging data as described previously (Zhan et al., 2014; Matsui et al., 2011). First, the EPIs were realigned and co-registered to a template brain using anatomical images. Owing to the lack in open-source anatomical brain images in young adult rats, we used a representative T2W anatomical image (P22) as a template brain. Co-registered functional EPIs were normalized to the template and transformed to a 151 × 91 × 81 matrix (with spatial resolution of 0.20 × 0.20 × 0.20 mm^3) and smoothed with a Gaussian kernel (full width at half maximum [FWHM], 0.7 mm). We manually omitted data with motion artifacts (26 scans in total). Imaging data were temporally zero-phase band-pass filtered to retain low-frequency components (0.01–0.10 Hz) by using the *filtfilt* MATLAB function. For a given time series, seed ROIs (0.8 × 0.8 × 0.6 mm^3) in the anterior lobe of the cerebellar vermis (CblVm), cerebellar hemispheres (CblHs), cerebellar dentate nuclei (CblNc), dorsal hippocampi (Hpc), primary visual cortices (V1), sensory cortices (S1), motor cortices (M1), cingulate cortices (Cg), medial prefrontal cortices (mPf), centro-medial thalamus (cmThl), and posterior thalami (pThl) were selected, and the signals in the seed were averaged. For CblHs, CblNc, Hpc, V1, S1, M1, Cg, mPf, and pThl, seeds were applied in both right and left hemispheres. Individual correlation maps (r map at the zeroth lag) were computed by cross-correlation against the mean seed-signal to signals of all the other voxels. Then, correlation maps were transformed to normally distributed z scores by Fisher's r-to-z transformation. Z-transformation was used to reflect the strength of spontaneous correlations more linearly at high r values. The resulting group maps were thresholded at $|r| > 0.1$, followed by a cluster-level multiple comparison correction at a significance level of $p < 0.001$ of one-sample t test with $K\alpha > 29$ voxels (Figure 6H). Seed-seed correlation matrices were calculated from all pairs among brain regions for each subject. The correlation matrix was z-transformed. One-sample *t test* matrix across experiments were thresholded at $p < 0.05$ and were corrected by Benjamini-Hochberg (BH) procedure to avoid the incorrect rejection of a true null hypothesis (a type I error) with a false discovery rate at $q = 0.05$. Mean seed-seed correlation z-matrix was filtered by the T-matrix from BH procedure and variance corrected color maps were shown (Figure 6I).

For the group independent component analysis (ICA) (Figure S7), we used the MELODIC toolbox in the FSL platform (Beckmann and Smith, 2005; Zerbi et al., 2015). Group ICA was done on the experimental groups (NC, HKGn, and HKGn+C87) to estimate a common set of components for all three cohorts, using multi-session temporal concatenation, and we then extracted 40 components from the pre-processed data described above. We used the set of spatial maps from the three-cohort-average analysis to generate subject-specific versions of the spatial maps, using dual regression. We then generated average-spatial maps for each group by one-sample t test using the randomize function of FSL (Winkler et al., 2014). The resulting maps were corrected for multiple comparisons using threshold-free cluster enhancement (Smith and Nichols, 2009). These representative maps are color-coded as a value of 1-p with a threshold of $p < 0.01$.

The extent of anesthesia is quite important for the functional connectivity. We carefully applied adequate concentration of isoflurane with inhalation at the level of 1%, which is conventionally used. However, as reported in Arancillo et al. (2015), 0.15 – 0.25% of isoflurane concentration halves both simple and complex spike of mouse Purkinje cells *in vivo*, while the firing rate does not become silent. Although we did not apply electrophysiological recording of the Purkinje cells *in vivo*, we consider that the reduction of Purkinje cell firing under anesthesia did exist. Maybe, that's why the functional connectivity in the control rats (NC) were not obvious, relative to rats with inflammation (Figures 6H–6J). Meanwhile, in rats injected the heat-killed Gram-negative bacteria, the functional connectivity between cerebellar vermis and prefrontal cortex was quite prominent. Therefore, our data suggested that, even under the suppression of Purkinje cell firing with isoflurane anesthesia, the inflammation of the anterior lobes enhanced the correlation of cerebello-cortical activity. In addition, isoflurane is known as an activator of GABAergic receptors which increases the tonic inhibition, while the exact mechanism of the action has not been clearly understood in the cerebellum. Please note that there remains a possibility of the involvement of the modulation of GABAergic synaptic activity by inflammation.

QUANTIFICATION AND STATISTICAL ANALYSIS

All data are presented as mean ± SEM. SEM indicates standard error of measurement within a group. Details regarding each statistical test, biological sample size (n), p value and statics can be found in the corresponding figure legends or in Table S3.

The "n" in figures represents the number of animals, cells, or experimental replication. Detail values and representation of the data number are as following: in Figure 1, all "n" indicate cells from more than 3 animals for each experiment; in Figure 2B, "n" indicate sampled images from 2 animals for each experiment (Control, 100 μg/ml, 250 μg/ml, 20 mg/ml of Ki20227 administration); in Figures 2C–2E, "n" indicate cells from more than 4 animals for each experiment; in

Figures 3A–3G and 3N–3S, "n" indicate cells from more than 3 animals for each experiment; in Figure 3I, "n" indicate sampled cerebella; in Figures 3K and 3M, "n" indicate sampled regions from 2 to 3 animals for each experiment; in Figure 4, all "n" indicate cells from more than 3 animals for each experiment; in Figure 5, all "n" indicate cells from more than 3 animals for each experiment; in Figure 6, all "n" indicate animals for each experiment. Please note that in the OF experiments, all parameters were obtained from identical animals, and that in the behavior battery test (MB, SC, FS, PSC, SN and BR) many of data were obtained from identical animals; in Figure 7, all "n" indicate animals for each experiment.

Data were collected and processed side by side in randomized order for all experiments; most analyses were routinely performed blind to the conditions of the experiments. Two-sided Mann-Whitney *U*-tests were used to compare data between two independent groups, except for the following: in Figure 2B, 6B–6E, 7, S5A, S5B, S5E, and S6B–S6K, we used the multiple comparison with Kruskal-Wallis test, with Bonferroni method or Fisher's least significant difference procedure. In Figures 2E and 5C–5G, we used the Wilcoxon signed-rank test between the mean normalized firing frequency at −1 to −5 min and at +25 to +30 min. In Figures 3K and 3M,

we used the Wilcoxon signed-rank test between the mean ΔATP at −6 to −2 min and at +20 to +28 min. In Figures S5D and S5F, we used the unpaired Student's t test (two-tailed, unequal distribution). $p < 0.05$ was considered statistically significant, unless otherwise stated. All boxplot graphs show interquartile range with centered bars as median, minima and maxima of all of the individual data. Overlapping red marks on boxes represent mean ± SEM. Other thresholds are provided for each relevant comparison. Outliers in experiments of open field test, with the number of zero to three in each group, were excluded under assumption of normality by Grubb's test. All statistical analyses were preformed using MATLAB.

DATA AND CODE AVAILABILITY

Source Data that support the findings of this study are available from the Lead Contact upon reasonable request. Custom MATLAB code for analyses of the spike counting, s/mEPSC event and rs-*f*MRI are available from the Lead Contact upon individual request.